Airborne sunphotometer measurements of aerosol optical depth and columnar water vapor during the Puerto Rico Dust Experiment, and comparison with land, aircraft, and satellite measurements

John M. Livingston[1]*, Philip B. Russell[2], Jeffrey S. Reid[3], Jens Redemann[4], Beat Schmid[4], Duane A. Allen[2], Omar Torres[5], Robert C. Levy[6], Lorraine A. Remer[7], Brent N. Holben[8], Alexander Smirnov[9], Oleg Dubovik[9], Ellsworth J. Welton[9], James R. Campbell[6], Jun Wang[10], Sundar A. Christopher[10]

[1]SRI International, 333 Ravenswood Avenue, Menlo Park, CA, 94025

[2]NASA Ames Research Center, Moffett Field, CA 94035-1000

[3]SPAWAR Systems Center San Diego, San Diego, CA

[4]Bay Area Environmental Research Institute, Sonoma, CA

[5]Joint Center for Earth Systems Technology, University of Maryland Baltimore County, Baltimore, MD

[6]Science Systems and Applications, Inc., Lanham, MD

[7]Laboratory for Atmospheres, NASA Goddard Space Flight Center, Greenbelt, MD

[8]Laboratory for Terrestrial Physics, NASA Goddard Space Flight Center, Greenbelt, MD

[9]Goddard Environmental Science and Technology Center, University of Maryland Baltimore County, and NASA Goddard Space Flight Center, Greenbelt, MD

[10]Department of Atmospheric Sciences, University of Alabama in Huntsville, Huntsville, Alabama

*corresponding author
E-mail: jlivingston@mail.arc.nasa.gov

10/10/2002 5:38:20 PM UT

Abstract

Analyses of aerosol optical depth (AOD) and columnar water vapor (CWV) measurements obtained with the six-channel NASA Ames Airborne Tracking Sunphotometer (AATS-6) mounted on a twin-engine aircraft during the summer 2000 Puerto Rico Dust Experiment are presented. In general, aerosol extinction values calculated from AATS-6 AOD measurements acquired during aircraft profiles up to 5 km ASL reproduce the vertical structure measured by coincident aircraft in-situ measurements of total aerosol number concentration. AATS-6 extinction retrievals also agree with corresponding values derived from ground-based lidar measurements for altitudes above the trade inversion. The spectral behavior of AOD within specific layers beneath the top of the aircraft profile is consistent with attenuation of incoming solar radiation by large dust particles or by dust plus sea salt, with mean Ångström wavelength exponents of ~0.20. Values of CWV calculated from profile measurements by AATS-6 at 941.9 nm and from aircraft in-situ measurements agree to within ~4% (0.13 g/cm^2). AATS-6 AOD values measured on the ground at Roosevelt Roads Naval Air Station and during low altitude aircraft runs over the adjacent Cabras Island aerosol/radiation ground site agree to within 0.004-0.030 with coincident data obtained with an AERONET Sun/sky radiometer located on Cabras Island. For the same observation times, AERONET retrievals of CWV exceed AATS-6 values by ~21%. AATS-6 AOD values measured during low altitude aircraft traverses over the ocean are compared with corresponding AOD values retrieved over water from upwelling radiance measurements by the MODIS, TOMS, and GOES-8 Imager satellite sensors, with mixed results.

1. Introduction

Three decades have elapsed since the first studies showed that significant quantities of African dust are transported across the tropical North Atlantic to the Caribbean region [Delany et al., 1967; Carlson and Prospero, 1972; Prospero and Carlson, 1972]. Subsequent investigations have confirmed that this transport of dust is a regular occurrence and peaks during summer [e.g., Karyampudi and Carlson, 1988; Westphal et al., 1987, 1988; Prospero, 1996a,b]. Numerous studies have investigated the radiative effects of dust [e.g., Carlson and Benjamin, 1980; Joseph, 1984; Tanré et al., 1984; Ackerman and Chung, 1992; Duce, 1995; Haywood et al., 2001a, 2001b], and it has been estimated that the magnitude of the direct radiative forcing by the anthropogenic fraction of dust is at least comparable to the forcing by other anthropogenic aerosols [Tegen et al., 1996; Sokolik and Toon, 1996; Diaz et al., 2001; Myhre and Stordal, 2001]. However, limited observational data on the spatial and temporal distribution of dust and large uncertainties in critical micro-physical, chemical, and optical dust properties have made it impossible to quantify the radiative effects of dust [e.g., Sokolik et al., 2001].

The Puerto Rico Dust Experiment (PRIDE) was conducted from 28 June through 24 July 2000 to characterize and understand the optical and physical properties and controlling factors of the dust aerosol transported across the Atlantic from Africa [Reid et al., 2002; and this issue (a)]. The primary research aircraft during PRIDE was a twin-engine Piper Navajo, which flew 21 science flights over the Caribbean region from its base at Roosevelt Roads Naval Air Station (18.25ºN, 65.64ºW) on the east coast of Puerto Rico. The six-channel NASA Ames Airborne Tracking Sunphotometer (AATS-6) was mounted on the Navajo and, with the exception of occasional obscuration of the sun by clouds, took continuous measurements of aerosol optical depth (AOD) during the flights. The goal of these measurements was to study the vertical and

spectral dependence of the optical depth of dust, which is critical for quantitative assessment of its radiative impact [Sokolik et al., 2001].

The AATS-6 has been operated successfully aboard a variety of aircraft platforms and from the ground in several stratospheric and tropospheric research studies since 1985 [Russell et al., 1986; Livingston and Russell, 1989; Pueschel and Livingston, 1990; Russell et al., 1993a,b; Russell et al., 1996; Hegg et al., 1997; Russell et al., 1999a,b; Schmid et al., 1999; Livingston et al., 2000; Schmid et al., 2001a,b; Schmid et al., 2002]. During PRIDE, AATS-6 measurements were taken during a variety of clean and dust aerosol loading conditions with near-surface mid-visible aerosol optical depths that ranged from 0.10 to 0.55. In this paper, we present vertical profiles of AATS-6 AOD, aerosol extinction, column water vapor (CWV), and water vapor density, in addition to AOD spectra for specific atmospheric layers. We compare selected AATS-6 AOD data with coincident or near-coincident measurements of AOD by in-situ and remote ground-based, aircraft, and satellite sensors, and we compare AATS-6 water vapor measurements with coincident ground-based and aircraft data.

2. Instrumentation

2.1. Airborne Sensors

2.1.1 Six-Channel NASA Ames Airborne Tracking Sunphotometer (AATS-6)

The AATS-6 [Matsumoto et al., 1987; Russell et al., 1993a] tracks the sun and measures the direct beam solar transmission through the earth's atmosphere in six spectral channels. Each channel consists of a doubly baffled entrance tube, interference filter, photodiode detector, and integral preamplifier. The entrance baffles define a detector field of view (FOV) with measured half angle of 1.85°. The six filter/detector/preamplifier sets are mounted in a common heat sink

maintained at 45° ± 1°C. During PRIDE, the filters were centered at wavelengths 380.1, 450.9, 525.7, 864.5, 941.9, and 1021.3 nm, with filter bandwidths (FWHM) of 5.0-5.8 nm. Solar tracking is achieved by azimuth and elevation stepper motors driven by error signals derived from a differential-shadowing sun sensor.

Calibration of the AATS-6 was performed by taking sunrise measurements at Mauna Loa Observatory for eight days during late May 2000 prior to PRIDE and for six days during mid-October 2000. In all channels except 941.9 nm, the Langley plot technique [e. g., Russell et al., 1993; Schmid and Wehrli, 1995] was used to derive the exoatmospheric detector voltages that are necessary for subsequent calculation of instantaneous optical depths. At 941.9 nm, because water vapor and aerosol are the primary attenuators and attenuation by water vapor does not follow Beer's Law, a modified Langley technique [Reagan et al., 1995; Michalsky et al., 1995; Schmid et al., 1996, 2001b] was used.

During flight, photodiode voltages were digitized at three Hz, averaged over three seconds, and recorded together with signal standard deviations and various ancillary data, including aircraft location and altitude from a Trimble SVeeSix Plus GPS receiver. A cloud-screening algorithm that uses a variety of rejection criteria was applied during post-flight data processing. The primary data rejection criterion is a high relative standard deviation, typically one percent of the mean signal, in the photodetector voltages measured over the three-second (nine-sample) averaging period. Although this screening works quite well in removing the majority of cloud events, it can fail for short-lived partial obscuration events and for optically thin homogeneous overlying cirrus [Livingston et al., 2000], as will be demonstrated in one of the data examples presented below.

AODs and associated uncertainties were calculated according to the methodology described in Russell et al. [1993a,b], and CWV estimates and uncertainties were derived using the methodology described by Schmid et al. [2001b]. The uncertainty expressions are based on standard texts for uncertainty propagation [Bevington and Robinson, 1992; Taylor and Kuyatt, 1994]. Columnar ozone amounts necessary for the calculation of AOD from total optical depth were taken from the Total Ozone Mapping Spectrometer (TOMS) mounted on the Earth Probe satellite. In addition to the corrections for Rayleigh scattering and O_3 absorption, it was necessary to apply corrections for NO_2, H_2O and O_2-O_2 absorption in some channels. Most cross-sections were computed using the Line-by-Line Radiative Transfer Model (LBLRTM) 5.21 [Clough and Iacono, 1995] and the ESA-WV H_2O line-list of Schermaul et al. [2001], as described by Schmid et al. [2002]. NO_2 and O_2-O_2 cross-sections not included in LBLRTM 5.21 were taken from Harder et al. [1997], Schneider et al. [1987], Greenblatt et al. [1990] and Michalsky et al. [1999]. NO_2 was assumed constant at $5x10^{15}$ molecules cm^{-2}.

Because sunphotometers have a nonzero field of view, they measure some diffuse light in addition to the direct solar beam. As a result, uncorrected sunphotometer measurements can overestimate direct-beam transmission and underestimate aerosol optical depth (AOD). We have quantified these diffuse light effects for the aerosols prevalent during PRIDE by calculating the AOD correction factors defined by the analytical formulation of Shiobara and Asano [1994] and Kinne et al. [1997]. The calculations use the AATS-6 FOV (half-angle 1.85°) and aerosol scattering phase functions retrieved from Sun and sky radiance measurements by AERONET for dust events in Puerto Rico during PRIDE (cf. Section 2.2.1 below) and at Cape Verde before PRIDE [Dubovik et al., 2002]. For these conditions the corrections range from a maximum of ~6% for the 380-nm measurements to a minimum of ~2% for the 1021-nm measurements. (To

illustrate, a 6% correction to an AOD of 0.3 is 0.018.) All AATS-6 AOD values presented in this paper have been corrected for diffuse light by applying these correction factors.

In addition to diffuse light corrections, AODs have also been corrected, where appropriate, to account for the high likelihood that during flight dirt (dust, sea salt, and/or other aerosol particles) accumulated on the external surface of the AATS-6 quartz window that protects the filter and detector optics. Such accumulation decreases the measured solar transmission and, if not taken into account, results in an overestimate of AOD. The procedure for calculating and correcting for this effect is explained in detail in the Appendix, but a brief summary is in order here. As noted below, the typical Navajo science flight consisted of the following chronological segments: a vertical profile through the marine boundary layer (MBL) and the Saharan Air Layer (SAL) to some altitude above the dust over the Cabras Island (~18.21°N, 65.6°W) aerosol/radiation ground site near Roosevelt Roads; a transit at or near maximum altitude to a relatively cloud-free region over the ocean 50-170 km away; a descent back into the marine boundary layer (MBL) for an extended near-surface traverse over ocean; a subsequent ascent to an altitude above the SAL; and, finally, descent back into Roosevelt Roads. In applying the transmission corrections, it was assumed that all dirt accumulation on the AATS-6 window occurred linearly with time during the aircraft's mid-flight near-surface ocean run, which means that no data acquired before the aircraft's descent back into the MBL required correction. Hence, transmission correction factors were calculated from differences observed in high altitude AOD spectra measured before and after the aircraft's near-surface ocean traverse. These factors were used to adjust calculated AODs on a flight-, time-, and wavelength-dependent basis. Mean maximum AOD corrections ranged from 0.015 to 0.029. Separate measurements of dirt transmission before and after cleaning the instrument window following several flights not only

confirmed the likelihood of dirt deposition at some time during most of these flights but also permitted exclusion of all data acquired on certain flights from the dirt correction procedure (due to a measure of no change in transmission). Finally, as explained in the Appendix, for all AOD values for which a dirt transmission correction was applied, the corresponding uncertainty limits span the range of values that would result if there were no accumulation of dirt on the instrument window or if all dirt is assumed to have been deposited immediately upon the aircraft's descent back into the MBL prior to the near-surface ocean run. This results in asymmetric uncertainty limits.

2.1.2. Other Navajo Instrumentation

In addition to the AATS-6, the Navajo carried basic meteorological instrumentation (static pressure, temperature and water vapor), solar spectral flux radiometers, and two optical particle counters (a Particle Measuring System Forward Scattering Spectrometer Probe: FSSP-100, and a Passive Cavity Aerosol Spectrometer Probe: PCASP-100X) mounted on the aircraft wingtips. The in-situ instruments are described in detail by Reid et al. [2002, and this issue (a)], and the solar spectral flux radiometers by Pilewskie et al. [this issue]. In this paper, we use measurements from the Rosemount temperature sensor (±0.3 C), the static pressure sensor (±0.2 mb), the EdgeTech chilled mirror dewpoint hygrometer (±0.5 C), and the FSSP-100, which nominally measures particle number concentration in 20 size bins from 0.75 to 18 μm particle diameter.

2.2. Ground-Based Sensors

2.2.1. AERONET

The Aerosol Robotic Network (AERONET) consists of automatic tracking sun photometer/sky radiometers located at over 100 ground sites around the world [Holben et al., 1998]. These instruments measure AOD and CWV, which are routinely archived together with retrieved values of aerosol size distribution and single scattering albedo [Holben et al., 1998, 2001; Eck et al., 2001; Dubovik et al., 2002] after application of the cloud screening and quality control procedures described by Smirnov et al. [2000a]. During PRIDE, an AERONET CIMEL sun/sky photometer was operated at the Cabras Island ground site. Measurements of spectral aerosol optical depth were acquired every fifteen minutes at eight wavelengths: 340, 380, 440, 500, 670, 870, 940 and 1020 nm.

2.2.2. NASA GSFC Micro-Pulse Lidar

MPL-Net [Welton et al., 2001] is a worldwide network of micro-pulse lidar (MPL) systems run by members of the Cloud and Aerosol Lidar Group at NASA Goddard Space Flight Center (GSFC). The MPL [Spinhirne et al., 1995] is a single channel (523 nm), semi-autonomous, eye-safe lidar system that was originally developed at GSFC and is used to determine the vertical structure of clouds and aerosols. During PRIDE, one of the MPL units was operated at the Cabras Island ground site, and data have been analyzed to produce vertical profiles of aerosol backscatter and extinction [Welton et al., 2002].

2.3. Satellite Sensors

2.3.1 MODIS

The Moderate-Resolution Imaging Spectroradiometer (MODIS) instrument was launched aboard the Earth Observing System's (EOS) Terra satellite on 18 December 1999. MODIS measures upwelling spectral radiance at the top of the atmosphere in a wide wavelength range from 0.41 to 14.24 μm. Aerosol optical thickness is routinely retrieved in seven spectral bands (0.47, 0.55, 0.67, 0.87, 1.24, 1.64, and 2.13 μm) at 10 km resolution over the ocean [Tanré et al., 1997; Martins et al., 2002; Levy et al., this issue], and in two channels (0.47 and 0.66 μm) plus one interpolated wavelength (0.55 μm) over land [Kaufman et al., 1997].

2.3.2 TOMS

The Total Ozone Mapping Spectrometer (TOMS) measures backscattered near ultraviolet radiation at wavelengths in the range 331-360 nm from aboard the Earth-Probe (EP) satellite. The TOMS aerosol inversion algorithm [Torres et al., 1998, 2002] uses measurements at two wavelengths to retrieve aerosol optical depth and one microphysical aerosol property such as effective particle size or refractive index (from which single scattering albedo is calculated).

2.3.3 GOES-8 Imager

The Geostationary Operational Environmental Satellite (GOES)-8 imager is the most recent in a series of geostationary satellite imagers that measures upwelling radiance at high temporal resolution. Measurements are taken in five spectral channels with half-power response bandwidths of 0.52-0.74 μm (Channel 1), 3.79-4.04 μm (channel 2), 6.47-7.06 μm (channel 3), 10.2-11.2 μm (channel 4), and 11.6-12.5 μm (channel 5). The sampled sub-point spatial resolution is 0.57 x 1 km for the visible channel and 2.3 x 4 km for the other channels [Menzel

and Purdom, 1994]. For the PRIDE study period, Wang et al. [this issue] have used half-hourly GOES-8 imager data in combination with a pre-calculated radiance/AOD lookup table approach [Zhang et al., 2001; Christopher and Zhang, 2002; Christopher et al., 2002] to retrieve dust AOD in the visible channel over the ocean.

3. Results

3.1. Aircraft Flight Pattern

The flight pattern was essentially the same for each of the 21 science flights flown by the Navajo. An example, the 21 July flight, is shown in Figure 1. Immediately after takeoff from Roosevelt Roads, power was provided to the various onboard science instruments. After all instruments were operational, the Navajo descended to about 30 m ASL and from that point performed a continuous ascent over the adjacent Cabras Island aerosol/radiation ground site to characterize the local environment. Generally, the maximum altitude (~4.0-5.5 km) of the ascent was a few hundred meters above the top of the major dust layer, which was determined using the real-time readout of particle number concentration measured by the FSSP and the meteorological state variables. Concurrent AOD measurements from the AATS-6 were available to confirm that at least the major portion of the attenuating aerosol overburden had been traversed.

Upon completion of the ascent, the aircraft headed at or near maximum altitude to a relatively cloud-free region over the ocean 50-170 km away, where a stepped descent was executed with intermittent level legs of ~10-15 km in length for taking in-situ particle size and spectral solar flux measurements. On most flights, the intial ascent and subsequent descent were timed to position the Navajo near the surface at the time of the Terra satellite overpass for validation of MODIS. Near satellite overpass time, the plane flew a low-level horizontal

traverse for approximately 20 minutes. This was followed by another ascent to an altitude of interest prior to final descent (not shown in Figure 1 example) back into Roosevelt Roads.

3.2. Vertical Profiles of AATS-6 Aerosol Optical Depth and Extinction

AATS-6 measurements of AOD were obtained from near surface to maximum altitude during the early flight ascent over the Cabras Island site on fourteen of the 21 flights. Data were partially affected by overlying cirrus during two of these fourteen. Clouds prevented any AATS-6 measurements on two of the Cabras ascents, and prevented measurements in the lowest 1-2 km on four others. There was no ascent over the site on one flight. The AOD profile measured during the 21 July ascent over Cabras is shown together with AOD spectra at selected aircraft altitudes in the bottom frames of Figure 1.

Each data point in the AOD spectral plot of Figure 1 represents the mean of five to 47 AATS-6 measurements, where each measurement is itself a nine-sample (three-sec) average, as discussed in Section 2.1.1 above. Two sets of vertical bars are overplotted on each data point. The bar with wide horizontal ticks equals the mean of the measurement uncertainties calculated according to Russell et al. [1993a,b] for each AATS-6 measurement included in the mean AOD value shown, and it represents our best estimate of the one standard deviation uncertainty in the data point. The corresponding bar with narrow horizontal ticks equals the sample standard deviation, and it is shown to provide a measure of the spatio-temporal atmospheric variability associated with the measurements. This method of presentation of two sets of vertical bars is used in subsequent figures where mean AATS-6 AOD values are shown. In all cases, the mean uncertainties exceed the sample standard deviations.

Figure 2 presents profiles of AOD spectra measured by the AATS-6 during eleven different flights, including eight early flight ascents, six descents, and two late flight ascents.

The profiles represent the range of AOD values and vertical aerosol distributions measured during the experiment. The Puerto Rico area was impacted by six significant dust events during PRIDE [Reid et al., 2002, and this issue (a)]. The first and strongest of the six arrived on June 28; others arrived on July 5, 9, 15, 21 and 23. At least one profile from each of these events except the July 9 case is shown in Figure 2.

Aerosol extinction profiles can be derived from the AOD profiles shown in Figures 1 and 2 by calculating the vertical derivative of AOD. In practice, we calculate extinction by first averaging AOD within 100-m bins, then fitting a smoothing cubic spline through the averaged AOD profile. The tension on the spline can be adjusted to control the amount of smoothing of the fit. The numerical derivative of this spline fit then yields a corresponding vertically smoothed aerosol extinction profile, as shown in the bottom right frame of Figure 1. This procedure is performed separately for each of the five aerosol wavelengths. Figure 3 overlays aerosol extinction profiles derived in this manner with profiles of aerosol number concentration and aerosol surface area calculated from the coincident FSSP particle size distribution measurements in ~100-m bins for the same profiles presented in Figure 2. In general, the vertical profiles in extinction, number, and area exhibit similar shapes, although the calculated AATS-6 extinction profiles are unable to resolve the fine structure observed by the in-situ sensor. The calculated FSSP total particle surface area concentration is more directly related, through the Mie extinction cross section, to the extinction coefficient than is total particle number concentration. However, calculated values of particle surface area concentration from the FSSP data are less certain than corresponding total particle number concentration because of instrumental uncertainties in the particle sizing [Collins et al., 2000; Reid et al., 2002, and this issue (b)].

In principle, it should be possible to quantify the spectral dependence of aerosol extinction as a function of height from our calculations. In practice, however, we had limited success in extracting useful quantitative information on the aerosol extinction spectral behavior from the AATS-6 PRIDE data set. We attribute this to a combination of effects: instrument tracking uncertainty during aircraft profiles and channel-to-channel FOV variations, small spatial inhomogeneities in dust AOD, which exhibits a relatively flat wavelength dependence (see Figure 4), and the extinction retrieval procedure, which is applied separately to spline fits to vertically smoothed measurements of AOD at each wavelength. We are confident that the spectral dependence of AOD at any given height is an accurate measure of the spectral dependence of the overlying aerosol, and that the general shape of the calculated extinction profile reflects the true distribution, but the uncertainty in the absolute magnitudes of the calculated extinction values combined with the relatively flat wavelength dependence of the dust prohibits the extraction of useful quantitative information on spectral aerosol extinction behavior with height. Extinction retrievals [e.g., Schmid et al., 2000, 2002] derived from profile measurements obtained with the next generation NASA Ames airborne sunphotometer, AATS-14, are better posed experimentally, as AATS-14 has a much improved tracking accuracy and FOV homogeneity.

For the PRIDE time frame, Reid et al. [2002] report a range of dust maximum altitudes from 2.3 to 5.2 km, as determined from the FSSP aerosol number concentrations. AATS-6 AOD and extinction profiles are consistent with these findings, and indicate that the vertical distribution of the dust, including the height of the dust layer and the distinctness of the layer top, varied significantly from event to event and, apparently, during the evolution of an event. For example, the corresponding AOD and extinction profiles measured during the two largest

dust outbreaks, June 28 and July 21, differ markedly between the two events. Profiles of extinction and FSSP number concentration measured on June 28 show a significant amount of dust below the trade inversion (1 km, Reid et al, [2002]), and up to at least 4 km. Aerosol extinction coefficients derived from the AATS-6 AOD measurements are ~0.25 km^{-1} near the surface, ~0.15 km^{-1} just above the trade inversion, and ~0.10 km^{-1} between 2 and 4 km. Corresponding values of aerosol number concentration range from ~17 cm^{-3} near the surface to ~8 cm^{-3} in the upper layer. As the event begins to wane on June 30, the concentration of dust decreases most significantly in the region below 2 km, but there remains a well-defined layer between 2 and 4 km, although maximum aerosol number concentration and extinction in that layer decrease to ~6 cm^{-3} and ~0.08 km^{-1}, respectively.

Analogous profiles for the July 21 ascent over Cabras Island and descent over the ocean ~30 km to the south (see flight track and selected data in Figure 1) reveal the presence of a broad dust layer up to 5 km, but with significantly less dust below 2 km compared to the June 28-30 event. Dust concentrations increase from ~5 cm^{-3} below the height of the trade inversion (~1.4 km for the early flight ascent) to a maximum of 10 cm^{-3} just below 5 km. The distribution includes a relative maximum at the height of the trade inversion and a well-defined clean layer with values as low as ~5 cm^{-3} at ~1.7 km altitude just above the inversion. The corresponding aerosol extinction profiles corroborate this structure. Mean values beneath the trade inversion are ~0.05 km^{-1}, with a relative maximum of 0.07-0.10 km^{-1} at the inversion height, and a relative minimum with values <0.05 km^{-1} just above. Above the thin clean layer, extinction increases with height to a maximum of ~0.12 km^{-1} at 4.5 km. The rapid decrease in dust concentration and extinction above the maximum on July 22 is dramatic. Measurements taken after the advent of another dust impulse the following day, July 23, reflect the spatio-temporal variability of the dust

distribution. Two profiles are shown for this day: the descent at 13.1-14.4 UT and the ascent 30-60 min later about 70 km to the NW. The evolution of this dust event can be seen in the next frame of Figure 2, in which AOD values on July 24 are approximately 50% less than the corresponding values on July 23. The shape of the vertical distribution of the dust appears to remain intact, as is shown in the corresponding aerosol extinction and FSSP number distribution profiles (Figure 3).

The dust event that arrived in Puerto Rico on July 15 is documented in Figures 2 and 3 for data acquired during aircraft descent on July 15 and during the aircraft ascent over Cabras Island and subsequent descent over the open ocean on July 16. The July 15 profile is particularly interesting, not only because of the dust distribution, but also because it includes intermittent solar attenuation by overlying thin cirrus that was not removed from the data by our cloud screening filters. The presence of cirrus is reflected in the "noisy" nature of the AOD profile at certain altitudes. However, cloud-free AOD measurements at various altitudes during this aircraft descent have enabled Pilewskie et al. [this issue] to combine the AOD data with coincident flux measurements acquired by the NASA Ames Solar Spectral Flux Radiometer and thereby to present a detailed analysis of the radiative characteristics of the dust aerosol for this case. Furthermore, despite the presence of some cirrus in the unsmoothed AOD measurements (Figure 2), the spline-smoothed AOD profile yields an aerosol extinction profile that is consistent with the FSSP aerosol number concentration profile, as shown in Figure 3. Subsequent profiles measured on July 16 are cloud free, and they provide a measure of the vertical distribution of the dust for this event that is consistent with the aerosol number concentration data.

Finally, we call attention to the data obtained during the descent on July 24. Since AOD must decrease with altitude for a horizontally homogeneous, time-invariant aerosol, the apparent increase in AOD with height that is observed in Figure 2 around 1.0 km altitude results from a horizontal or temporal change in attenuation along the sunphotometer's moving line of sight during the profile, as does any increase in AOD with altitude in any of the profiles shown. Since this descent was observed to be cloud-free, this apparent increase in AOD with altitude is indicative of horizontal or temporal variation of the aerosol. Although the AOD profile clearly shows a spectral dependence below 1.5 km, the spectral dependence and, in fact, the absolute magnitudes of the calculated extinction values cannot be verified precisely because of this apparent increase in AOD with altitude and its effect on the subsequent spline fits and calculated extinction.

3.3. Wavelength Dependence of Aerosol Optical Depth

For each measurement day during PRIDE, Reid et al. [2002] have published values for the height of the trade inversion and the height of the Saharan Air Layer (SAL) top, where the SAL is defined as the layer between the trade inversion (determined from the meteorological data) and the SAL top (determined from the FSSP number concentration data and the state variables). We have calculated AOD spectra for selected layers for one AOD profile on each day when AATS-6 obtained measurements from profile bottom to profile top. These layers were defined as the entire profile (profile bottom to profile top), the bottom of the profile to the height of the trade inversion, and the SAL. Layer AOD values were determined by differencing mean AOD values calculated within 20 m of the profile bottom, and within 50 m of the heights of the trade inversion and the SAL top. The spectral dependence of aerosol optical thickness in the visible spectrum is often approximated by a power law relation [Ångström, 1964],

$$\tau(\lambda) = \tau(\lambda_0)\left(\frac{\lambda}{\lambda_0}\right)^{-\alpha} \qquad (1)$$

where τ is AOD, λ is wavelength, and α is the Ångström exponent. We apply standard unweighted linear least squares fitting methodology over the five AATS-6 aerosol wavelengths (380-1021 nm) to calculate an effective Ångström exponent for layer AOD spectra. These results are presented in Figure 4 for those cases for which the SAL AOD at 525-nm wavelength was at least 0.01. Within each layer, AOD exhibits a relatively flat spectral dependence, with mean α values of 0.19-0.21, and sample standard deviations 0.08-0.17. These α values are consistent with the range of values (calculated using AOD at two wavelengths only) reported for dust by Smirnov et al., [2000b] for ground-based AERONET data taken on Barbados, by Sabbah et al. [2001] for ground-based handheld sunphotometer measurements in Egypt, and by Tanré et al. [2001] and Dubovik et al. [2002] for AERONET data taken at three sites in and around the African continent. For our data set, the largest standard deviation is found in the layer below the trade inversion, which probably reflects the presence of non-dust (maritime or pollution) aerosol, although this cannot be determined from AATS-6 data.

3.4. Comparison of AATS-6 and MPL Aerosol Extinction Profiles

Aerosol extinction profiles derived from AATS-6 measurements at 525.7 nm taken during aircraft ascents over Cabras Island on four days (6, 13, 16 and 21 July) have been compared with corresponding profiles derived from near-coincident aerosol backscatter measurements by the Cabras Island GSFC MPL. These profiles are shown in Figure 5 together with coincident profiles of aerosol surface area concentration measured by the Navajo FSSP. For July 6, 13 and 16, each MPL extinction profile shown is the average of all profiles (two or

three) measured during the time of the Navajo ascent. Individual profiles were derived using the MPL-Net operational level 2.0 data processing algorithm and represent a 20 minute cloud-screened signal average centered on the coincident (Cabras Island) AERONET observation time. Each is derived from a measured backscatter profile by applying a height-independent extinction-to-backscatter ratio that is calculated from the vertically integrated MPL backscatter profile and the AERONET CIMEL sunphotometer AOD measurement. This procedure also calculates the MPL calibration value. The dashed lines give the mean uncertainties for the individual profiles included in the average. The July 21 profile is the average of several lidar profiles measured during the period 1200-1600 UT. Coincident MPL and AERONET observations were not available during this overflight; therefore, the extinction profile was generated using a calibration value extrapolated from the nearest MPL-Net level 2.0 data (approximately 1 hour before and after the overflight times).

For three of the four cases shown in Figure 5, the agreement between MPL and AATS-6 extinction is better above 1-1.5 km than below this level. This is likely because the MPL aerosol extinction profile is derived from a single, height-independent backscatter-to-extinction ratio for which the backscatter and extinction are dominated by aerosol (dust) above the trade inversion. The peaks in MPL aerosol extinction below 1.0 km may be due to elevated aerosol concentrations near clouds at the top of the MBL. The FSSP aerosol surface area profiles more closely reproduce the vertical structure measured by the MPL than do the AATS-6 extinction profiles. This is not surprising since the FSSP essentially measures particle concentration at each altitude and the data shown have been binned over 100 m, whereas the basic AATS-6 measurement describes the overlying column (transmission or AOD), and extinction is derived from this column AOD through smoothing and numerical differentiation, as discussed above.

3.5. AATS-6 Water Vapor Measurements

As noted above, solar transmittance measurements in the AATS-6 941.9-nm channel permit calculation of columnar water vapor [Schmid et al., 2001a,b; Livingston et al., 2000]. Subsequent vertical differentiation of CWV measured during aircraft profiles yields values of water vapor density. Figure 6 presents AATS-6 values of CWV (green) and water vapor density (blue) for the same profiles shown in Figures 2 and 3. Also shown for comparison are values of water vapor density (red) calculated from coincident Navajo measurements of temperature, static pressure, and dewpoint (EdgeTech hygrometer) averaged within 100-m bins. Water vapor density has been derived from the AATS-6 CWV profiles in a manner analogous to that used to calculate aerosol extinction from the AATS-6 AOD profiles. First, mean CWV values are calculated by averaging within 20-m altitude bins. These mean values are shown in Figure 6 together with uncertainty limits (bars) that include all sources of measurement uncertainty [c.f., Schmid et al., 1996]; the standard deviations of the data within the 20-m bins are much smaller than the uncertainties and are not shown. Each mean CWV profile is smoothed further using a cubic spline fit. Finally, the resultant smoothed profile is numerically differentiated to yield a water vapor density profile. Qualitatively, the AATS-6 retrievals yield the same general vertical structure measured by the hygrometer. Below 3.5 km, rms differences for the 16 profiles shown in Figure 6 range from 6% to 17%, but there are significant differences (e.g., gross overestimate or underestimate of density near the surface by AATS-6) that we attribute to effects of aerosol or water vapor variability during profiling on the AATS-6 CWV retrieval procedure. Note that the hygrometer water vapor density values represent averages within ~100-m bins and are subject to measurement uncertainties in pressure (±0.2 mb), temperature (±0.3 C) and dewpoint (±0.5 C) that lead to estimated water vapor density uncertainties of 0.3-0.6 g/m^3 below ~2.0 km.

Because AATS-6 water vapor density represents a second order product, a comparison of corresponding AATS-6 and aircraft in-situ water vapor density profiles can provide a skewed view of the agreement or lack thereof. As noted, the primary water vapor product derived from AATS-6 measurements in the 941.9-nm channel is CWV. The total CWV within the aircraft profile follows directly from the AATS-6 measurements by differencing the values at the bottom and the top of the profile. Corresponding profile CWV amounts can be calculated as a second order product of the aircraft in-situ water vapor measurements by numerically integrating the hygrometer water vapor density profile.

Figure 7 compares profile CWV amounts calculated from the AATS-6 and the hygrometer measurements. Results are shown separately for fifteen early-flight Navajo ascents (blue) over the Cabras Island ground site (7a), seventeen subsequent descents (green) over the open ocean (7b), ten ascents (red) over open ocean (7c), and the composite set (7d). The solid line in each frame represents a one-to-one correspondence. Rms differences are 0.22 g/cm^2 (~6%) for each set of profiles, and mean differences (AATS-6 minus hygrometer) range from –0.12 to –0.14 g/cm^2 (–3.3% to –4.1%). In part, these differences may arise because a single profile CWV value retrieved from the in-situ measurements is an integral quantity that includes spatio-temporal variability over the entire profile, whereas the AATS-6 value is calculated as the difference between two measurements (mean CWV at bottom minus mean CWV at top) separated in time and space. Clearly, any spatio-temporal change in water vapor overburden between the top and bottom of the profile would be reflected in the AATS-6 CWV result, but any variability encountered during the time period between when the aircraft was at the top and when the aircraft was at the bottom would not be reflected in the single AATS-6 value.

3.6. Comparison of AATS-6 and AERONET AOD and CWV

AATS-6 measurements of AOD and total CWV can be compared with coincident AERONET measurements for those cases when the Navajo flew over the Cabras Island ground site at a minimum aircraft altitude of ~30 m. Unfortunately, due to the frequent occurrence of clouds, there were only four cases when near temporally coincident (within one hour) measurements are available for direct comparison. AOD spectra for these cases are presented in Figure 8. The spectral signatures are similar and AODs agree in magnitude to within the uncertainties. No adjustment has been applied to AATS-6 AOD to account for the small amount (~0.001-0.003) of AOD in the layer between the Cimel at the surface and the aircraft minimum altitude. Figure 9 presents a scatter plot of AOD at adjacent wavelengths, except that AATS-6 data at 451 nm and 526 nm have been interpolated to the AERONET wavelengths of 440 nm and 500 nm, respectively. AODs exhibit rms differences that range from 0.004 (~2%) at 1020 nm to 0.016 (6.6%) at 380 nm. Corresponding CWV values are shown in the last frame of Figure 9. Over the 3.0-4.5 g/cm^2 range of CWV values measured, AERONET values exceed AATS-6 values by about 0.76 g/cm^2 (~23%).

Twelve additional cases have been identified for comparison of the AERONET measurements and AATS-6 measurements taken while the Navajo aircraft was on the ground at Roosevelt Roads NAS airport. The corresponding AOD spectra and AOD and CWV scatter plots are presented in Figures 10 and 11, respectively. Although the instruments were separated by ~5.6 km, all measurements shown were acquired within 10 minutes of each other. AOD spectra agree to within rms differences that range from 0.014 (8%) at 1020 nm to 0.031 (13.5%) at 380 nm. The CWV results are similar to those for the Cabras Island flybys, with AERONET CWV exceeding AATS-6 values by about 0.73 g/cm^2 (~21%).

The disagreement between AATS-6 and AERONET CWV values probably results from differences in the spectroscopic models used to relate slant path water vapor transmission measurements to corresponding CWV amounts for the AATS-6 and AERONET instruments. The AATS-6 PRIDE CWV retrievals use LBLRTM 5.21 with the Schermaul et al. [2001] ESA H_2O line list, while AERONET retrievals [Holben et al., 1998] use LOWTRAN 7 [Kneizys et al., 1996], which includes an early version of the HITRAN database [Rothman et al., 1998]. Previous work [Schmid et al., 2001b] has shown that using the same model and spectroscopy for an AERONET Cimel and ground-based AATS-6 CWV measurements leads to agreement within 3%. It can be shown that switching from LOWTRAN 7 to LBLRTM 5.21 with the ESA H_2O line list decreases the retrieved CWV by about 20% [Giver et al., 2000; Belmiloud et al., 2000; Schmid et al., 2001a,b], which is the difference between the CWV values derived from the Roosevelt Roads AATS-6 and AERONET measurements during PRIDE.

3.7. Comparison of AATS-6 and Satellite AOD Measurements

The advantage of spaceborne sensors to provide near-global spatial and near-continuous temporal observation of the Earth-atmosphere system is well documented [e.g., King et al., 1999]. However, there is an ongoing critical need to validate these satellite measurements using ground-based and airborne in-situ and remotely sensing instruments. The wide geographical distribution of AERONET radiometers [Holben et al., 1998] has proven invaluable for providing long-term ground-based measurements of aerosol optical thickness and other columnar aerosol size distribution scattering properties for satellite validation. Although subject to the spatial and temporal limitations of the aircraft on which it is mounted and, of course, to the vagaries of overlying clouds, an airborne sunphotometer is capable of yielding vertically-resolved profiles of aerosol extinction during aircraft ascents and descents, as discussed above, and of providing a

direct measure of AOD variability along horizontal flight legs near the ocean surface. Each of these additional pieces of information can be extremely valuable for satellite sensor validation. In this section, we compare AATS-6 AOD measurements acquired at altitudes within 30-130 m of the ocean surface with corresponding values of AOD retrieved from coincident upwelling radiance measurements taken by MODIS, TOMS and the GOES-8 imager for selected cases.

3.7.1. Comparison of AATS-6 and MODIS AOD

Recent studies by Chu et al. [2002] and Remer et al. [2002] have discussed validation of MODIS aerosol products over land and over ocean, respectively. Ichoku et al. [2002] have developed a spatio-temporal approach that they applied to validation of MODIS aerosol retrievals using data from the over 100 ground AERONET sites. Levy et al. [this issue] present a detailed comparison of MODIS aerosol retrievals with aircraft and ground-based sunphotometer measurements during PRIDE. In our paper, we compare AATS-6 and MODIS AODs for four moderate to high dust load cases and three low aerosol load cases. Data from these cases are included in Levy et al. [this issue].

Figure 12 compares AATS-6 and MODIS AOD spectra for each of the seven cases. Each of the first three frames includes one dust case and one relatively "clean" case; the last frame shows only a dust case. Each MODIS data point represents a mean over an area, 5 pixels by 5 pixels, where each pixel is about 10 km by 10 km. (Total area is 50 km x 50 km resolution). Vertical bars with wide ticks display the expected MODIS retrieval uncertainty $\Delta\tau$, where $\Delta\tau = \pm 0.03 \pm 0.05\tau$ [Remer et al., 2002; Ichoku et al., 2002], and those with narrow ticks show the sample standard deviation of MODIS AOD retrievals within the 5 by 5 pixel box. The solid lines connect the MODIS spectral values. Each AATS-6 data point is the mean of all cloud-filtered measurements taken over a 3-12 minute low altitude (30-130 m ASL) horizontal transect

over the ocean surface near or including the time of the Terra satellite overpass. The dashed lines are second order polynomial fits of AOD versus wavelength in log-log space. Measurement uncertainties and sample standard deviations are shown by wide and narrow ticks, respectively.

It is clear from examination of Figure 12 that the current MODIS aerosol retrieval algorithm overestimates the spectral dependence of AOD for the moderate to high dust load cases, resulting in significant overestimates of AOD at short wavelengths, primarily. The explanation for this discrepancy is thought to lie in the inability of the current MODIS algorithm to treat correctly the scattering by irregularly shaped dust particles [Levy et al., this issue]. For the three low aerosol load events the MODIS AOD wavelength dependence is closer to the AATS-6 wavelength dependence, but MODIS AODs exceed AATS-6 AODs for the two cleanest cases, July 11 and July 19, and underestimate the AATS-6 AOD for the July 12 case. For these cases, values do agree within combined experimental uncertainties, however.

Figure 13 shows the ensemble comparison of MODIS and AATS-6 AOD at the four shortest MODIS wavelengths, where the AATS-6 values have been interpolated to the MODIS wavelengths using the fits shown in Figure 12. The MODIS AOD uncertainty limits are the same as those shown with wide ticks in Figure12; the AATS-6 AOD uncertainty limits are calculated from those displayed in Figure 12 (wide ticks) by linear interpolation in linear(uncertainty)-log(wavelength) space. The solid line depicts a one-to-one correspondence. The low and high aerosol load cases form two distinct groups in Figure 13, and the MODIS tendency to overestimate sunphotometer AOD at the shortest wavelengths for the high load dust events is also evident.

3.7.2. Comparison of AATS-6 and TOMS AOD

The TOMS family of sensors has provided measurements of backscattered near ultraviolet radiation for over two decades [Heath et al., 1975]. The initial objective of the TOMS instrument was to provide accurate global estimates of total column ozone. In recent years, studies by a number of investigators have used differences in backscattered radiances measured in the near UV by TOMS to detect absorbing aerosols [e.g., Hsu et al., 1996; Seftor et al., 1997; Herman et al., 1997; Gleason et al, 1999; Chiapello et al., 1999]. Torres et al. [1998] showed that by using an ensemble of aerosol models it is possible to derive values of aerosol optical depth and single scattering albedo from TOMS near UV measurements. Most recently, Torres et al. [2002] used TOMS data to derive a long-term record of AOD over the oceans and the continents, and used AERONET ground-based AOD observations to conduct an in-depth comparison of the validity of TOMS AOD retrievals over land.

During PRIDE, the Earth Probe-TOMS (EP-TOMS) satellite overflew the general study area between ~1400 and 1600 UT each day. Values of AOD and single scattering albedo at 380 nm have been retrieved from the TOMS measurements using the "Direct Method" and dust aerosol models described by Torres et al. [1998, 2002]. Near-surface AATS-6 measurements were acquired near the time of satellite overpass during twelve of the 21 Navajo science flights, so initially these twelve cases were identified as possible targets of opportunity for comparison of AATS-6 and TOMS AOD retrievals. However, by restricting the analysis to cases where TOMS and AATS-6 measurements were collocated within one degree latitude and one degree longitude and occurred within one hour of each other, the number of cases was reduced to five. These have been analyzed in detail, and the results are presented in Figure 14 for all TOMS pixels centered within 150 km of the AATS-6 mean location. Figure 14a is a scatterplot of the

retrieved AODs. Open symbols display retrievals for which the measured reflectance indicates likely sub-pixel cloud contamination based on the combined use of reflectance and Aerosol Index thresholds used as cloud mask in the TOMS algorithm [Torres et al., 2002]; solid symbols show acceptable cloud-free retrievals. Numbers beside the data points indicate the spatial separation (in km) of TOMS and AATS-6 measurements, and the TOMS-retrieved single scattering albedo. Vertical bars show the TOMS AODretrieval uncertainty, which is the larger of 0.1 or 20% for non-absorbing aerosols, and 0.1 or 30% for absorbing aerosols [Torres et al., 2002]. Horizontal bars display AATS-6 AOD measurement uncertainties; sample standard deviations (not shown) are 0.003-0.008. In Figure 14b, AOD differences (TOMS minus AATS-6) corresponding to the data presented in Figure 14a are plotted as symbols, and combined (root-sum-square) AATS-6 and TOMS AOD uncertainties are shown by vertical bars.

AATS-6 AOD values range from 0.11 (19 July) to 0.53 (21 July) for the five cases shown in Figure 14. For the 10 July case, the AATS-6 AOD is 0.23, and the retrieved TOMS AOD is 0.19 for the closest (65 km) TOMS pixel. The retrieved single scattering albedo of 0.97 indicates that the aerosol was only weakly absorbing at 380 nm. The TOMS AOD of 0.10 for the second closest pixel (85 km) is less than half the AATS-6 AOD, but this pixel may represent background aerosol, as the aerosol was non-absorbing. TOMS retrievals for the 19 July case also indicate a weakly absorbing aerosol, with AOD values of 0.12 and 0.21, compared to the AATS-6 AOD of 0.11. For the 20 July case, retrievals are shown for five TOMS pixels, but three (shown with open symbols) are probably cloud contaminated since they are right at the edge of the cloud mask. The two cloud-free retrievals agree with the AATS-6 AOD, 0.34, within the combined uncertainty. The 21 July case represents the largest AATS-6 AOD, 0.53, and includes the most absorbing aerosol at 380 nm of the five cases shown, with TOMS retrieved

single scattering albedos of 0.79-0.94. Based on the TOMS cloud mask, the closest (33 km) of the seven pixels might have been slightly cloud-contaminated, but cloud free conditions clearly prevailed in the other six pixels. TOMS AOD retrievals within four of the seven pixels agree with the AATS-6 value within combined uncertainty. TOMS AODs for the 22 July comparison range from 0.09 to 0.34, compared to 0.24 for AATS-6, but three of the four retrievals agree to within the combined uncertainty. The aerosol on this day was non-absorbing or very weakly absorbing at 380 nm.

3.7.3. Comparison of AATS-6 and GOES-8 Imager AOD

Figure 15 compares AATS-6 near-surface AOD measurements with corresponding values calculated from GOES-8 imager measurements in the visible channel (0.52-0.74 μm) during ten satellite observations (nine days). Each AATS-6 data point represents a one-minute average bracketing the time of satellite observation and has been interpolated to 0.670 μm, the approximate center wavelength of the GOES-8 visible channel. Each GOES-8 data point is a mean of all retrievals for cloud-free pixels within a box defined by the range of Navajo locations included in the AATS-6 average for that particular satellite observation. GOES-8 AOD uncertainties (bars with wide ticks) are ±0.06 [Wang et al., this issue]; sample standard deviations (bars with narrow ticks) are 0.05-0.11. AATS-6 uncertainties are 0.02-0.03, while sample standard deviations are 0.005-0.013. AOD differences (GOES-8 minus AATS-6) and combined uncertainties are plotted in Figure 15b. The data yield an r^2 of 0.70, but rms differences are 0.12 (41%) and GOES-8 AOD retrievals overestimate AATS-6 AODs by a mean value of 0.09 (31%). Only five of ten data points agree within the combined uncertainty.

During the Navajo's near-surface traverse over the ocean on 10 July, a gradient of ~0.1 in AOD over ~0.25° in latitude was measured by AATS-6. Figure 16 compares AATS-6 AODs

(interpolated to 670 nm) measured during the time period 1521 UT (latitude 18.2°) - 1533 UT (latitude 17.8°) with corresponding AODs retrieved from GOES-8 670-nm data acquired during the satellite observation at 1545 UT. GOES-8 data points were calculated as follows. First, the range of latitudes (18.2° - 17.8°) covered by the Navajo during the 1521-1533 UT period was divided into 60 evenly spaced intervals. Then, for each latitude interval, GOES-8 AOD retrievals were averaged for all apparent cloud-free pixels located within ±0.015° (~±1.75 km) latitude and ±0.06° (~±6.75 km) longitude of the Navajo flight track. The 0.12°-longitude range corresponds to twice the maximum longitude range covered by the Navajo during the entire time period. The number of pixels included in each average ranged from 63 to 75. For the GOES-8 retrievals, dashed lines display the sample standard deviation of the data points included in each average, and the dotted lines show the mean AOD uncertainty of ±0.06 [Wang et al., this issue]. The AATS-6 data points are the standard (*cf.* Section 2.1.1) three-sec (nine-sample) averages, and the uncertainty band represents the Russell et al. [1993a,b] measurement uncertainties. The two instruments appear to have observed the same general latitudinal gradient in AOD, at least between 17.85° and ~18.07° latitude. However, GOES-8 AOD spatial standard deviations are comparable to the GOES-8 AOD uncertainty of ±0.06, which includes a large GOES-8 calibration uncertainty [Zhang et al., 2001; Wang et al, this issue] and GOES-8 retrieval model uncertainty. Possible sub-pixel cloud contamination is not accounted for in the uncertainty propagation.

4. Summary and Concluding Remarks

During the summer 2000 Puerto Rico Dust Experiment, airborne measurements of AOD and CWV were acquired with the AATS-6 on 21 research flights that originated from Roosevelt

Roads Naval Air Station and typically extended as far as 100-140 km over the Caribbean. These measurements have yielded valuable information on the vertical distribution and spectral dependence of dust transported from Africa. Profiles of AOD and CWV obtained during aircraft ascents and descents in the vicinity of Puerto Rico have been presented, as have corresponding profiles of aerosol extinction and water vapor density calculated from the measured AOD and CWV profiles. AOD layer spectra have been calculated for the entire vertical column, for the layer between the surface and the top of the trade inversion, and for the SAL, and all have been found to exhibit a relatively flat spectral dependence, with mean Ångström exponents of ~0.20, consistent with attenuation of the incoming solar radiation by dust or dust plus sea salt. AATS-6 data have been compared with coincident or near-coincident measurements by aircraft in-situ sensors and by ground-based remote sensors.

Aerosol extinction profiles calculated from the AATS-6 AOD data exhibit the same general vertical structure measured by coincident FSSP aerosol size distribution measurements of total aerosol number and surface area concentration, but the AATS-6 extinction retrievals are unable to reproduce the fine-scale structure seen by the FSSP. We found similar results in a comparison of AATS-6 and MPL aerosol extinction profiles calculated from coincident measurements acquired during four aircraft profiles over the Cabras Island MPL site. For each of those cases, AATS-6 and MPL extinction values agree well above the trade inversion where dust dominated the height-independent aerosol backscatter-to-extinction ratio used to derive extinction from the MPL backscatter data.

AATS-6 measurements of CWV within the vertical column sampled by the aircraft have been shown to agree to within an rms difference of ~0.2 g/cm^2 (~6%) with corresponding values of CWV calculated from the aircraft measurements of temperature, pressure, and dewpoint. For

the composite set of 42 separate profiles, AATS-6 CWV values underestimate the in-situ values by a mean value of ~0.13 g/cm^2 (~4%). In general, vertical profiles of sunphotometer-derived water vapor density agree with corresponding values calculated from the in-situ measurements to within rms differences of 6-17% below 3.5 km, although significant differences do occur near the surface for some cases. These differences reflect both the smoothing and numerical differentiation procedure applied to the AATS-6 data and the spatio-temporal atmospheric variability during profiling.

AATS-6 spectral AOD measurements acquired during low-altitude aircraft flybys of the Cabras Island aerosol/radiation ground site and during separate ground-based measurement periods at Roosevelt Roads NAS airport have been compared with coincident AERONET measurements taken at Cabras Island. Values agree to within rms differences of 0.004 (at 1020 nm) to 0.016 (at 380 nm) for the flybys and 0.014 (1020 nm) to 0.031 (380 nm) for the ground measurements. The larger differences for the ground-based comparisons are likely due to horizontal inhomogeneities and to the 5.6-km separation between the instruments. However, AERONET CWV values exceeded AATS-6 CWV values by ~0.73 g/cm^2 (~21% of mean CWV of ~3.5 g cm^{-2}), which is attributed to differences in the spectroscopy used to relate the sunphotometer measurements of solar transmission in the water vapor channel to CWV for the two instruments.

AATS-6 measurements have been used in limited satellite sensor validation exercises for data acquired over the ocean. In particular, AATS-6 AODs measured during low-altitude aircraft traverses have been compared with corresponding values derived from coincident or near-coincident measurements by MODIS, TOMS, and the GOES-8 imager, with varying levels of agreement.

For measured moderate to high load dust cases (AATS-6 mid-visible AODs of ~0.25-0.35), the current MODIS aerosol algorithm retrieves AODs with a spectral dependence significantly steeper than that of the corresponding AATS-6 measurements. Specifically, MODIS AOD retrievals overestimate measured AATS-6 values in the visible and underestimate AATS-6 values in the near IR. Levy et al. [this issue] have attributed this result to the inability of the algorithm to handle scattering by irregularly shaped particles. The agreement is somewhat better for three low or no dust load cases (AATS-6 mid-visible AODs 0.07-0.10). For these cases, MODIS retrievals fall within the combined uncertainties for data from the two instruments, but mean values from MODIS underestimate AATS-6 AOD for 11 July and overestimate AATS-6 AOD for 12 July.

Near-surface AOD measurements in the AATS-6 380.1-nm channel have been compared with TOMS AOD retrievals at 380 nm for five cases with AATS-6 AODs that ranged from 0.11 to 0.53. For each case, AOD retrievals have been shown for all TOMS pixels within 150 km and one hour of the AATS-6 measurements. After rejection of TOMS retrievals in those pixels for which the TOMS cloud mask indicates likely sub-pixel cloud contamination, almost 70% (11 of 16) of the remaining retrievals agree with AATS-6 data to within the combined one-sigma measurement uncertainty. However, it should be noted that TOMS AOD retrieval uncertainties are the larger of 0.1 or 30% of AOD for absorbing aerosols.

AOD values retrieved from the GOES-8 visible imager data during ten satellite overflights have been compared with coincident AATS-6 near-surface measurements. The rms difference is 0.12 (41%), and GOES-8 retrievals overestimate AATS-6 measured AODs by ~0.09 (31%) at the GOES-8 mean wavelength, 670 nm. Only 50% (5 of 10) retrievals agree within the combined one-sigma uncertainty. GOES-8 appears to have observed the same general latitudinal

AOD gradient (~0.1) measured by AATS-6 on 10 July, although GOES-8 AOD uncertainties and spatial standard deviations are large.

The results of the satellite validation exercise underscore the need for continued comparison of satellite retrievals of over-ocean AOD with aircraft measurements to improve satellite retrieval algorithms. The large variability in the magnitude and spatio-temporal distribution of dust AOD that AATS-6 measured during PRIDE highlights the importance of airborne sunphotometer AOD data for making such comparisons. Additional work remains to quantify further the effects of particle shape, intra-scene spatial variability of the aerosol, and sub-pixel cloud contamination on retrieved satellite products. Future studies and/or analyses should focus on these problems.

Appendix. Procedure for calculating and correcting for the effect of dirt on the external surface of the AATS-6 optics window

The presence of dirt (dust and/or sea salt) on the external surface of the AATS-6 quartz window that protects the filter and detector optics decreases the measured solar transmission and, if not taken into account, results in an overestimate of AOD. Two pieces of evidence led us to conclude that dirt sometimes accumulated on the window during flight. The first comes from ground-based measurements taken before and after cleaning the window immediately after landing. Due to clouds, these measurements were taken after only eleven flights. Although dirt was not visible on the window prior to cleaning (with the exception of one flight during which the instrument remained exposed to the air stream during a traverse through the remnant of a cirrus anvil), these measurements yielded mean transmission reductions due to dirt of 2.0-3.4%, with the largest single flight decrease of 7.6% for one channel only. The second piece of

evidence comes from measurements of high altitude AOD spectra before and after the near-surface ocean traverse. For ten of eleven flights for which these measurements were available, the data indicate an increase in high altitude AOD (before any correction due to the possible presence of window dirt) following the near-surface ocean run. The one exception yields constant AOD and is a flight during which overlying thin cirrus was observed. Mean AOD increases derived from the high altitude spectral measurements were 0.015-0.029 for AOD values of 0.01-0.06 at the top of the early flight ascent. Although the two high altitude (top of ascent) AOD spectra were typically separated by about two hours and 30-120 km for a particular flight, if it is assumed that the observed increases in AOD were caused solely by the accumulation of dirt on the instrument window, then they correspond to transmission reductions due to dirt of 1.5-2.9%.

Because the results we present use only in-flight measurements taken during or before the top of the late flight ascent (in fact, all comparisons with satellite measurements use only data acquired during the mid-flight near-surface ocean run), we apply AOD dirt transmission correction factors based on the measured differences in the high altitude AOD spectra. The largest sources of uncertainty in correcting for dirt are (1) we have no data on exactly when the dirt deposited on the window for any flight, and (2) about half the flights have no measurement of a high altitude AOD spectrum after the ocean run or of window dirt transmission after the flight. Recognizing these uncertainties, we have applied a dirt transmission correction in the following manner. For all flights, it has been assumed that the instrument became cold soaked at the top of the aircraft's intial ascent above the SAL and that dirt began to accumulate on the optics window only after the aircraft subsequently descended into the moist MBL below the trade inversion (a value of 1.0 km has been assumed for this purpose). It has been assumed

further that dirt continued to accumulate linearly (resulting in a linear decrease in transmission) with time during the aircraft's flight leg within the MBL until it climbed above 1.0 km during a subsequent ascent or until the end of AATS-6 data acquisition for those flights during which the aircraft never flew above 1.0 km following the ocean run. The amount of dirt (hence, dirt transmission) was assumed to remain constant throughout the remainder of the flight. For those flights where high altitude data were available following the ocean run, the minimum dirt transmissions (maximum dirt accumulation) were set equal to the wavelength-dependent dirt transmissions derived from the high altitude AOD spectra measured before and after the near-surface run. For those flights where no post-ocean run high altitude spectrum was obtained, the maximum decrease in measured transmission due to dirt was assumed to be 50% of the mean values calculated from the data acquired on those flights when two high altitude spectra were measured. For those cases where post-flight measurements indicated no decrease in transmission before and after window cleaning, no dirt transmission corrections were applied. In all cases where a dirt transmission correction has been applied, the uncertainty limits in AOD span the range of values that would result from an assumption of no dirt (upper bar) and from an assumption that all dirt (lower bar) was deposited as soon as the aircraft descended through 1.0 km altitude following its initial ascent above the dust.

Acknowledgments. Financial support for the measurements and analyses was provided by the Office of Naval Research (Program Code 622-43-00-53-21), and by NASA's Earth Observing System Inter-Disciplinary Science (EOS-IDS) and Total Ozone Monitoring System (TOMS) Programs (Program Codes 291-01-91-45 and 621-14-01-00, respectively). We thank the Ozone

Processing Team at NASA Goddard Space Flight Center for making available TOMS Earth Probe ozone data.

References

Ackerman, S. A., and H. Chung, Radiative effects of airborne dust on regional energy budgets at the top of the atmosphere., *J. Appl. Meteorol*., *31*, 223-233, 1992.

Ångström, A., The parameters of atmospheric turbidity, *Tellus*, *16*, 64-75, 1964.

Belmiloud, D., R. Schermaul, K. M. Smith, N. F. Zobov, J. W. Brault, R. C. M. Learner, D. A. Newhnam, and J. Tennyson, New studies of the visible and near-infrared absorption by water vapour and some problems with the HITRAN database, *Geophys. Res. Lett.*, *27*, 3703-3706, 2000.

Bevington, P. R., and D. K. Robinson, *Data Reduction and Error Analysis for the Physical Sciences*, 328 pp., WCB/McGraw-Hill, Boston, MA., 1969.

Carlson, T. N., and J. M. Prospero, The large-scale movement of Saharan air outreaks over the northern equatorial Atlantic, *J. Appl. Meteorol*., *11*, 283-297, 1972.

Carlson, T. N., and S. G. Benjamin, Radiative heating rates of Saharan dust, *J. Atmos. Sci*., *37*, 193-213, 1980.

Chiapello, I., J. M. Prospero, J. R. Herman, and N. C. Hsu, 1999, Detection of mineral dust over the North Atlantic Ocean and Africa with the Nimbus 7 TOMS, *J. Geophys. Res.*, *104*, 9277-9291, 1999.

Christopher, S. A., and J. Zhang, Daytime variation of shortwave direct radiative forcing of bimass burning aerosols from GOES 8 imager, *J. Atmos. Sci*., GACP special issue, *59(2)*, 681-691, 2002.

Christopher, S. A., J. Zhang, B. N. Holben, and S-K. Yang, GOES-8 and NOAA-14 AVHRR retrieval of smoke aerosol optical thickness during SCAR-B, *Int. J. Rem. Sens*., in press, 2002.

Chu, D. A., Y. J. Kaufman, C. Ichoku, L. A. Remer, D. Tanre, and B. N. Holben, Validation of MODIS aerosol optical depth retrieval over land, *Geophys. Res. Lett*., in press, 2002.

Clough, S. A., and M. J. Iacono, Line-by-line calculations of atmospheric fluxes and cooling rates II: Application to carbon dioxide, ozone, methane, nitrous oxide, and the halocarbons, *J. Geophys. Res.*, *100*, 16,519-16,535, 1995.

Collins, D. R., H. H. Jonsson, J. H. Seinfeld, R. C. Flagan, S. Gassó, D. A. Hegg, P. B. Russell, B. Schmid, J. M. Livingston, E. Öström, K. J. Noone, L. M. Russell, and J. P. Putaud., In

situ aerosol size distributions and clear column radiative closure during ACE-2, *Tellus*, *52B*, 498-525, 2000.

Delany, A. C., D. W. Parkin, J. J. Griffin, E. D. Goldberg, and B. E. F. Reinman, Airborne dust collected at Barbados, *Geochim. Cosmochim. Acta*, *31*, 885-909, 1967.

Díaz, J. P., F. J. Expósito, C. J. Torres, and Félix Herrera, Radiative properties of aerosols in Saharan dust outbreaks using ground-based and satellite data: Applications to radiative forcing, *J. Geophys. Res.*, *106*, 18,403-18,416, 2001.

Dubovik, O., B. Holben, T. F. Eck, A. Smirnov, Y. J. Kaufman, M. D. King, D. Tanré, and I. Slutsker, Variability of absorption and optical properties of key aerosol types observed in worldwide locations, *J. Atmos. Sci*., *59*, 590-608, 2002.

Duce, R. A., Sources, distributions, and fluxes of mineral aerosols and their relationship to climate, in *Aerosol Forcing of Climate*, edited by R. J. Charlson and J. Heintzenberg, pp. 43-72, John Wiley, New York, 1995.

Eck, T. F., B. N. Holben, D. E. Ward, O. Dubovik, J. S. Reid, A. Smirnov, M. M. Mukelabai, N. C. Hsu, N. T. O'Neill, and I. Slutsker, Characterization of biomass burning aerosols in Zambia during the 1997 ZIBBEE field campaign, *J. Geophys. Res*., *106*, 3425-3448, 2001.

Gleason, J. F., N. C. Hsu, and O. Torres, Biomass burning smoke measured using backscattered ultraviolet radiation: SCAR-B and Brazilian smoke interannual variability, *J. Geophys. Res.*, *103*, 31,969-31,978, 1998.

Greenblatt, G. D., J. J. Orlando, J. B. Burkholder, and A. R. Ravishhankara, Absorption measurements of oxygen between 330 and 1140 nm, *J. Geophys. Res.*, *95*, 18,577-18,582, 1990.

Harder, J. W., J. W. Brault, P. V. Johnston, and G. H. Mount, Temperature dependent NO_2 cross sections at high spectral resolution, *J. Geophys. Res.*, *102*, 3861-3879, 1997.

Haywood, J. M., P. N. Francis, M. D. Glew, and J. P. Taylor, Optical properties and direct radiative effect of Saharan dust: A case study of two Saharan dust outbreaks using aircraft data, *J. Geophys. Res.*, *106*, 18,417-18,430, 2001a.

Haywood, J. M., P. N. Francis, I. Geogdzhayev, M. Mishchenko, and R. Frey, Comparison of Saharan dust aerosol optical depths retrieved using aircraft mounted pyranometers and 2-channel AVHRR algorithms, *Geophys. Res. Lett*., *28*, 2393-2396, 2001b.

Heath, D. F., A. J. Krueger, H. R. Roeder, and B. D. Henderson, The solar backscatter ultraviolet and total ozone mapping spectrometer (SBUV/TOMS) for Nimbus G., *Opt. En*g., *14*, 323-331, 1975.

Hegg, D. A., J. M. Livingston, P. V. Hobbs, T. Novakov, and P. B. Russell, Chemical apportionment of aerosol column optical depth off the mid-Atlantic coast of the United States, *J. Geophys. Res.*, *102*, 25,293-25,303, 1997.

Holben, B. N., T. F. Eck, I. Slutsker, D. Tanré, J. P. Buis, A. Setzer, E. Vermote, J. A. Reagan, Y. J. Kaufman, T. Nakajima, F. Lavenu, I. Jankowiak and A. Smirnov, AERONET—A federated instrument network and data archive for aerosol characterization, *Rem. Sens. Environ*., *66*, 1-16, 1998.

Holben, B. N., D. Tanré, A. Smirnov, T. F. Eck, I. Slutsker, N. Abuhassan, W. W. Newcomb, J. Schafer, B. Chatenet, F. Lavenue, Y. J. Kaufman, J. Vande Castle, A. Setzer, B. Markham, D. Clark, R. Frouin, R. Halthore, A. Karnieli, N. T. O'Neill, C. Pietras, R. T. Pinker, K. Voss, and G. Zibordi, An emerging ground-based aerosol climatology, Aerosol optical depth from AERONET, *J. Geophys. Res.*, *106*, 12,067-12,097, 2001.

Hsu, N. C., J. R. Herman, J. F. Gleason, O. Torres, and C. J. Seftor, Satellite detection of smoke aerosols over a snow/ice surface by TOMS, *Geophys. Res. Lett*., *26*, 1165-1168, 1999.

Ichoku, C., D.A. Chu, S. Mattoo, L.A. Remer, Y.J. Kaufman, D. Tanré, and B. Holben, A spatio-temporal approach for the validation of MODIS aerosol and water vapor products, *Geophys. Res. Lett*., in press, 2002.

Joseph, J. H., The sensitivity of a numerical model of the global atmosphere to the presence of desert aerosol, in *Aerosols and Their Climatic Effects*, edited by H. E. Gerber and A. Deepak, pp. 215-226, A. Deepak, Hampton, Va., 1984.

Karyampudi, V. M., and T. N. Carlson, Analysis and numerical simulations of the Saharan air layer and its effects on easterly wave disturbances, *J. Atmos. Sci*., *45*, 3102-3136, 1988.

Kaufman, Y. J., D. Tanré, L. A. Remer, E. F. Vermote, A. Chu and B. N. Holben, Operational remote sensing of tropospheric aerosol over land from EOS moderate resolution imaging spectroradiometer, *J. Geophys. Res*., *102*, 17,051-17,067, 1995.

King, M. D., Y. J. Kaufman, D. Tanre, and T. Nakajima, Remote sensing of tropospheric aerosols from space: past, present, and future, *Bull. Amer. Meteor. Soc., 80,* 2229-2259, 1999.

Kinne, S., T. P. Ackerman, M. Shiobara, A. Uchiyama, A. J. Heymsfield, L. Milosevich, Wendell, E. W. Eloranta, C. Purgold, and R. W. Bergstrom, Cirrus cloud radiative and microphysical properties from ground observations and in situ measurements during FIRE 1991 and their application to exhibit problems in cirrus solar radiative transfer modeling, *J. Atmos. Sci.*, 54, 2320-2344, 1997.

Kneizys F.X., L.W. Abreu, G. P. Anderson, J.H. Chetwynd, E.P. Shettle, A. Berk, L.S. Bernstein, D.C. Robertson, P. Acharaya, L.S. Rothmann, J.E.A. Selby, W.O. Gallery, and S.A. Clough, "The MODTRAN 2/3 Report and LOWTRAN 7 Model", 11 Jan. 1996, Phillips Laboratory, Geophysics Directorate PL/GPOS, 29 Randolph Road, Hanscom AFB, MA 01731-3010.

Levy, R. C., L. A. Remer, D. Tanre, Y. J. Kaufman, B. N. Holben, J. M. Livingston, P. B. Russell, H. Maring, and C. Ichoku, Validation of the MODIS retrievals of dust aerosol over the ocean during PRIDE, *J. Geophys. Res*., this issue.

Livingston, J. M., and P. B. Russell, Comparison of satellite-inferred (SAGE II) AODs with corresponding airborne sun-photometer optical depths. Preprint AIAA 27th Aerospace Sciences Meeting, January 9-12, 1989, Reno, Nevada.

Livingston, J. M., V. N. Kapustin, B. Schmid, P. B. Russell, P. K. Quinn, T. S. Bates, P. A. Durkee, P. J. Smith, V. Freudenthaler, M. Wiegner, D. S. Covert, S. Gassó, D. Hegg, D. R. Collins, R. C. Flagan, J. H. Seinfeld, V. Vitale, and C. Tomasi, Shipboard sunphotometer measurements of aerosol optical depth spectra and columnar water vapor during ACE-2, and comparison with selected land, ship, aircraft, and satellite measurements, *Tellus*, *52B*, 594-619, 2000.

Martins, J.V., D. Tanré, L. Remer, Y. Kaufman, S. Mattoo and R. Levy, MODIS cloud screening for remote sensing of aerosol over ocean using spatial variability, *Geophys. Res. Lett*., in press, 2002.

Matsumoto, T., P. B. Russell, C. Mina, and W. Van Ark, Airborne tracking sunphotometer, *J. Atmos. Oceanic Technol*., *4*, 336-339, 1987.

Menzel, W. P., and J. F. Purdom, Introducing GOES-I: The first of a new generation of geostationary operational environmental satellites, *Bull. Amer. Meteor. Soc., 75*, 757-781, 1994.

Michalsky, J. J., J. C. Liljegren, and L. C. Harrison, A comparison of sun photometer derivations of total column water vapor and ozone to standard measures of same at the Southern Great Plains Atmospheric Radiation Measurement site, *J. Geophys. Res*., *100*, 25,995-26,003, 1995.

Michalsky, J., M. Beauharnois, J. Berndt, L. Harrison, P. Kiedron, and Q. Min, O_2-O_2 absorption band identification based on optical depth spectra of the visible and near-infrared, *Geophys. Res. Lett*., *26*, 1581-1584, 1999.

Moulin, C., H. R. Gordon, V. F. Banzon, and R. H. Evans, Assessment of Saharan dust absorption in the visible from SeaWiFS imagery, *J. Geophys. Res. 106*, 18,239-18,249, 2001.

Murayama, T., N. Sugimoto, I. Uno, K. Kinoshita, K. Aoki, N. Hagiwara, Z. Liu, I. Matsui, T. Sakai, T. Shibata, K. Arao, B.-J. Sohn, J. G. Won, S.-C. Yoon, T. Li, J. Zhou, H. Hu, M. Abo, K. Iokibe, R. Koga, and Y. Iwasaka, Ground-based network observation of Asian dust events of April 1998 in east Asia, *J. Geophys. Res*., 106, 18,345-18,359, 2001.

Myhre, G., and F. Stordal, Global sensitivity experiments of the radiative forcing due to mineral aerosols, *J. Geophys. Res*., *106*, 18,193-18,204, 2001.

Pilewskie, P., R. Bergstrom, et al., Solar spectral radiative forcing by dust aerosol during the Puerto Rico Dust Experiment, *J. Geophys. Res*., this issue.

Prospero, J. M., and T. N. Carlson, Vertical and areal distribution of Saharan dust over the western equatorial North Atlantic Ocean, *J. Geophys. Res*., *77*, 5255-5265, 1972.

Prospero, J. M., The atmospheric transport of particles to the ocean, in *Particle Flux in the Ocean*, edited by V. Ittekkott, S. Honjo, and P. J. Depetris, pp. 19-52, John Wiley, 1996a.

Prospero, J. M., Saharan dust transport over the north Atlantic Ocean and Mediterranean: An overview, in *The Impact of Desert Dust Across the Mediterranean*, edited by S. Guerzoni, and R. Chester, pp. 133-151, Kluwer Acad., Norwell, Mass., 1996b.

Pueschel, R. F., and J. M. Livingston, Aerosol spectral optical depth: Jet fuel and forest fire smokes, *J. Geophys. Res*., *95*, 22,417-22,422, 1990.

Reagan, J., K. Thome, B. Herman, R. Stone, J. Deluisi, and J. Snider, A comparison of columnar water-vapor retrievals obtained with near-IR solar radiometer and microwave radiometer measurements, *J. Appl. Meteorol*., *34*, 1384-1391, 1995.

Reid, J. S., D. L. Westphal, J. M. Livingston, D. L. Savoie, H. B. Maring, H. H. Jonsson, D. P. Eleuterio, and J. E. Kinney, Dust vertical distribution in the Caribbean during the Puerto Rico Dust Experiment, *Geophys. Res. Lett*., in press, 2002.

Reid, J. S., D. L. Westphal, J. M. Livingston, H. H. Jonsson, J. E. Kinney, E. J. Welton, A. A. Smirnov, M. Meier, D. L. Savoie, H. B. Maring, S. C. Tsay, S. Christopher, D. P. Eleuterio, and E. A. Reid, Measurements of Saharan dust by airborne and ground-based remote sensing methods during the Puerto Rico Dust Experiment (PRIDE), *J. Geophys. Res*., this issue (a).

Reid, J. S., H. H. Jonsson, H. B. Maring, A. A. Smirnov, D. L. Savoie, S. S. Cliff, M. M. Meier, and D. L. Westphal, Understanding the size and morphological measurements of coarse mode dust particles from Africa, *J. Geophys. Res*., this issue (b).

Remer, L. A., D. Tanre, Y. J. Kaufman, C. Ichoku, S. Mattoo, R. Levy, D. A. Chu, B. N. Holben, O. Dubovik, A. Smirnov, J. V. Martins, R-R. Li, and Z. Ahmad, Validation of MODIS aerosol retrieval over land, *Geophys. Res. Lett*., in press, 2002.

L. S. Rothman, C. P. Rinsland, A. Goldman, S. T. Massie, D. P. Edwards, J.-M. Flaud, A. Perrin, C. Camy-Peyret, V. Dana, J.-Y. Mandin, J. Schroeder, A. McCann, R. R. Gamache, R. B. Wattson, K. Yoshino, K. V. Chance, K. W. Jucks, L. R. Brown, V. Nemtchinov, and P. Varanasi, The HITRAN Molecular Spectroscopic Database and HAWKS (HITRAN Atmospheric Workstation): 1996 Edition, *J. Quant. Spectr. Rad. Transf*., *60*, 665-710, 1998.

Russell, P. B., T. Matsumoto, V. J. Banta, J. M. Livingston, C. Mina, D. S. Colburn, and R. F. Pueschel, Measurements with an airborne, autotracking, external-head sunphotometer, *Preprint Volume, Sixth Conference on Atmospheric Radiation, May 13-16, 1986*, pp. 55-58, Amer. Meteor. Soc., Boston, MA, 1986.

Russell, P. B., J. M. Livingston, E. G. Dutton, R. F. Pueschel, J. A. Reagan, T. E. DeFoor, M. A. Box, D. Allen, P. Pilewskie, B. M. Herman, S. A. Kinne, and D. J. Hofmann, Pinatubo and pre-Pinatubo optical-depth spectra: Mauna Loa measurements, comparisons, inferred particle size distributions, radiative effects, and relationship to lidar data, *J. Geophys. Res*., *98*, 22,969-22,985, 1993a.

Russell, P. B., J. M. Livingston, R. F. Pueschel, J. A. Reagan, E. V. Browell, G. C. Toon, P. A. Newman, M. R. Schoeberl, L. R. Lait, L. Pfister, Q. Gao, and B. M. Herman, Post-

Pinatubo optical depth spectra vs. latitude and vortex structure: Airborne tracking sunphotometer measurements in AASE II, *Geophys. Res. Lett*., *20*, 2571-2574, 1993b.

Russell, P. B., J. M. Livingston, R. F. Pueschel, J. J. Bauman, J. B. Pollack, S. L. Brooks, P. Hamill, L. W. Thomason, L. L. Stowe, T. Deshler, E. G. Dutton, and R. W. Bergstrom, Global to microscale evolution of the Pinatubo volcanic aerosol derived from diverse measurements and analyses, , *J. Geophys. Res*., *101*, 18,745-18,763, 1996.

Russell, P. B., Hobbs, P. V. and Stowe, L. L., Aerosol properties and radiative effects in the United States east coast haze plume: An overview of the Tropospheric Aerosol Radiative Forcing Observational Experiment (TARFOX), *J. Geophys. Res*., *104*, 2,213-2,222, 1999a.

Russell, P. B., J. M. Livingston, P. Hignett, S. Kinne, J. Wong, and P. V. Hobbs, Aerosol-induced radiative flux changes off the United States Mid-Atlantic coast: Comparison of values calculated from sunphotometer and in situ data with those measured by airborne pyranometer, *J. Geophys. Res*., *104*, 2,289-2,307, 1999b.

Sabbah, I., C. Ichoku, Y. J. Kaufman, and L. Remer, Full year cycle of desert dust spectral optical thickness and precipitable water vapor over Alexandria, Egypt, *J. Geophys. Res*., *106*, 18,305-18,316, 2001.

Schermaul, R., R. C. M. Learner, D. A. Newnham, R. G. Williams, J. Ballard, N. F. Zobov, D. Belmiloud, and J. Tennyson, The water vapor spectrum in the region 8600 – 15000 cm^{-1}; Experimental and theoretical studies for a new spectral line database. II: Linelist construction, *J. Mol. Spectrosc*., *208*, 43-50, 2001.

Schmid, B., and C. Wehrli, Comparison of sun photometer calibration by Langley technique and standard lamp*, Appl. Opt*., *34*, 4500-4512, 1995.

Schmid, B., K. J. Thome, P. Demoulin, R. Peter, C. Matzler, and J. Sekler, Comparison of modeled and empirical approaches for retrieving columnar water vapor from solar transmittance measurements in the 0.94-mm region, *J. Geophys. Res*., *101*, 9345-9358, 1996.

Schmid, B., J. Michalsky, R. Halthore, M. Beauharnois, L. Harrison, J. Livingston, P. Russell, B. Holben, T. Eck, and A. Smirnov, Comparison of aerosol optical depth from four solar radiometers during the fall 1997 ARM Intensive Observation Period, *Geophys. Res. Lett*., *26*, 2725-2728, 1999.

Schmid, B., J. M. Livingston, P. B. Russell, P. A. Durkee, H. H. Jonsson, D. R. Collins, R. C. Flagan, J. H. Seinfeld, S. Gassó, D. A. Hegg, E. Öström, K. J. Noone, E. J. Welton, K. Voss, H. R. Gordon, P. Formenti, and M. O. Andreae, Clear sky closure studies of lower tropospheric aerosol and water vapor during ACE-2 using airborne sunphotometer, airborne in-situ, space-borne, and ground-based measurements, *Tellus*, *52B*, 568-593, 2000.

Schmid B., Eilers, J.A., McIntosh, D.M., Longo, K., Livingston, J.M., Redemann, J., Russell, P.B., Braun, J., and Rocken, C., Sunphotometric measurement of columnar H_2O and aerosol optical depth during the 3rd Water Vapor IOP in Fall 2000 at the SGP ARM Site, *Proceedings of the 11th ARM Program Science Team Meeting*, Atlanta, Georgia, March 19-23, 2001a.

Schmid, B., J. J. Michalsky, D. W. Slater, J. C. Barnard, R. N. Hathore, J. C. Liljegren, B. N. Holben, T. F. Eck, J. M. Livingston, P. B. Russell, T. Ingold, and I. Slutsker, Comparison of columnar water-vapor measurements from solar transmittance methods, *Appl. Opt.*, *40*, 1886-1896, 2001b.

Schmid, B., J. Redemann, P. B. Russell, P. V. Hobbs, D. L. Hlavka, M. J. McGill, B. N. Holben, E. J. Welton, J. Campbell, O. Torres, R. A. Kahn, D. J. Diner, M. C. Helmlinger, D. A. Chu, C. Robles Gonzalez, and G. De Leeuw, Coordinated airborne, spaceborne, and ground-based measurements of massive, thick aerosol layers during the dry season in Southern Africa, in press, 2002.

Schneider, W., G. K. Moortgat, G. S. Tyndall, and J. P. Burrows, Absorption cross-sections of NO2 in the uv and visible region (200-700 nm) at 298 K, *J. Photochem. Photobiol., A: Chem.*, *40*, 195-217, 1987.

Seftor, C. J., N. C. Hsu, J. R. Herman, P. K. Bhartia, O. Torres, W. I. Rose, D. J. Scheider, and N. Krotkov, Detection of volcanic ash clouds from Nimbus 7/total ozone mapping spectrometer, *J. Geophys. Res*., *102*, 16,749-16,759, 1997.

Shiobara, M., and S. Asano, Estimation of Cirrus optical thickness from Sun photometer measurements, *J. Appl. Meteor*, 33, 672-681, 1994.

Smirnov, A., B. N. Holben, T. F. Eck, O. Dubovik, and I. Slutsker, Cloud screening and quality control algorithms for the AERONET data base, *Remote Sens. Env*iron. *73*, 73,337-73,349, 2000a.

Smirnov, A., B. N. Holben, D. Savoie, J. M. Prospero, Y. J. Kaufman, D. Tanre, T. F. Eck, and I. Slutsker, Relationship between column aerosol optical thickness and in situ ground based dust concentrations over Barbados, *Geophys. Res. Lett*., *27*, 1643-1646, 2000b.

Sokolik, I. N., and O. B. Toon, Direct radiative forcing by anthropogenic mineral aerosols, *Nature*, *381*, 681-683, 1996.

Sokolik, I. N., D. M. Winker, G. Bergametti, D. A. Gillette, G. Carmichael, Y. J. Kaufman, L. Gomes, L. Schuetz, and J. E. Penner, Introduction to special section: Outstanding problems in quantifying the radiative impacts of mineral dust, *J. Geophys. Res*., *106*, 18,015-18,027, 2001.

Spinhirne, J. D., J. A. R. Rall, and V. S. Scott, "Compact eye-safe lidar systems", *Rev. Laser Eng*., *23*, 26-32, 1995.

Tanré, D., J. F. Geleyn, and J. Slingo, First results of the introduction of an advanced aerosol-radiation interaction in the ECMWF low resolution global model, in *Aerosols and Their Climatic Effects*, edited by H. E. Gerber and A. Deepak, pp. 133-177, A. Deepak, Hampton, Va., 1984.

Tanré, D., Y. J. Kaufman, M. Herman, and S. Mattoo, Remote sensing of aerosol properties over oceans using MODIS/EOS spectral radiances, *J. Geophys. Res*., 102, 16,971-16,988, 1997.

Tanré, D., Y. J. Kaufman, B. N. Holben, B. Chatenet, A. Karnieli, F. Lavenu, L. Blarel, O. Dubovik, L. A. Remer, and A. Smirnov, Climatology of dust aerosol size distribution and optical properties derived from remotely sensed data in the solar spectrum, *J. Geophys. Res*., *106*, 18,205-18,217, 2001.

Taylor, B. N., and C. E. Kuyatt, *Guidelines for Evaluating and Expressing the Uncertainty of NIST Measurement Results*, NIST Tech. Note 1297, U.S. Government Printing Office, Washington, D. C., 1994.

Tegen, I., A. A. Lacis, and I. Fung, The influence on climate forcing of mineral aerosols from disturbed soils, *Nature*, *380*, 419-422, 1996.

Torres, O., P. K. Bhartia, J. R. Herman, Z. Ahmad, and J. Gleason, Derivation of aerosol properties from satellite measurements of backscattered ultraviolet radiation: Theoretical basis, *J. Geophys. Res*., 103, 17,099-17,110, 1998.

Torres, O., P. K. Bhartia, J. R. Herman, A. Sinyuk, P. Ginoux, and B. Holben, A long-term record of aerosol optical depth from TOMS observations and comparison to AERONET measurements, *J. Atmos. Sci.*, *59*, 398-413, 2002.

Wang, J., S. A. Christopher, J. S. Reid, H. Maring, B. H. Holben, and S. K. Yang, GOES-8 retrieval of dust aerosol optical thickness over the Atlantic Ocean during PRIDE *, J. Geophys. Res.,* this issue.

Westphal, D. L., O. B. Toon, and T. N. Carlson, A two-dimensional numerical investigation of the dynamics and microphysics of Saharan dust storms, *J. Geophys. Res.*, *92*, 3027-3049, 1987.

Westphal, D. L., O. B. Toon, and T. N. Carlson, A case study of mobilization and transport of Saharan dust, *J. Atmos. Sci*., *45,*52145-2175, 1988.

Welton, E. J., J. R. Campbell, J. D. Spinhirne, and V. S. Scott, Global monitoring of clouds and aerosols using a network of micro-pulse lidar systems, in Lidar Remote Sensing for Industry and Environmental Monitoring, U. N. Singh, T. Itabe, N. Sugimoto, (eds.), *Proc. SPIE*, *4153*, 151-158, 2001.

Welton, E.J., K.J. Voss, P.K. Quinn, P.J. Flatau, K. Markowicz, J.R. Campbell, J.D. Spinhirne, H.R. Gordon, and J.E. Johnson, Measurements of aerosol vertical profiles and optical properties during INDOEX 1999 using micro-pulse lidars, *J. Geophys. Res*., in press, 2002.

Zhang, J., S. A. Christopher, and B. Holben, Intercomparison of aerosol optical thickness derived from GOES-8 Imager and Ground-Based Sun Photometers*, J. Geophys. Res., 106*, 7387-7398, 2001.

FIGURE CAPTIONS

Figure 1 Navajo flight profile and AATS-6 measurements for 21 July 2000. Bottom three frames show measured aerosol optical depth spectra with 2nd order polynomial fits at various altitudes and vertical profiles of measured aerosol optical depth and derived aerosol extinction.

Figure 2 Vertical profiles of aerosol optical depth measured by AATS-6 during Navajo ascents and descents.

Figure 3 Vertical profiles of aerosol extinction (color) calculated from the aerosol optical depth profiles shown in Figure 2; overlays of coincident aircraft-mounted FSSP measurements of aerosol number (thin black, 0-20 scale) and surface area (thick black, 0-600 scale) concentration.

Figure 4 Aerosol optical depth layer spectra measured (a) for the entire profile sampled by the Navajo, (b) for the Saharan Air Layer, and (c) for the layer from the bottom of the profile to the top of the trade inversion.

Figure 5 Comparison of aerosol extinction calculated from AATS-6 measurements (green) at 525.7 nm during ascents over the Cabras Island aerosol/radiation ground site and corresponding extinction (solid red) calculated from coincident backscatter measurements by the GSFC micro-pulse lidar located at the Cabras site; overlay of coincident total aerosol surface area concentration (solid black) measured by the FSSP aboard the Navajo. Dashed red lines are mean measurement uncertainties in the MPL profiles.

Figure 6 Vertical profiles of columnar water vapor (green) and water vapor density (blue) measured by AATS-6 for the same flights shown in Figures 2 and 3; corresponding profiles of water vapor density (red) calculated from the aircraft in-situ measurements of pressure, temperature and dewpoint (EdgeTech hygrometer).

Figure 7 Comparison of columnar water vapor measured by AATS-6 and EdgeTech hygrometer during aircraft ascents and descents.

Figure 8 Comparison of aerosol optical depth spectra measured by AATS-6 and ground-based AERONET CIMEL during Navajo overflights of Cabras Island aerosol/radiation ground site.

Figure 9 Scatterplots of aerosol optical depth and columnar water vapor measured by AATS-6 and ground-based AERONET CIMEL for the cases shown in Figure 8.

Figure 10 Comparison of ground-based measurements of aerosol optical depth spectra from the AERONET CIMEL at Cabras Island and the AATS-6 at Roosevelt Roads NAS.

Figure 11 Scatterplots of aerosol optical depth and columnar water vapor measured by AATS-6 and ground-based AERONET CIMEL for the cases shown in Figure 10.

Figure 12 Aerosol optical depth spectra measured by AATS-6 during aircraft horizontal flight legs at altitudes 30-100 m above the ocean surface, and corresponding spectra retrieved from coincident MODIS measurements. Dashed lines are quadratic fits to AATS-6 AOD spectra in log-log space. Solid lines merely connect the MODIS data points. Vertical bars with wide ticks are expected (MODIS) or calculated (AATS-6) measurement uncertainties; bars with narrow ticks are the spatio-temporal sample standard deviations.

Figure 13 For the data shown in Figure 12, scatterplot of MODIS aerosol optical depth retrievals and coincident AATS-6 aerosol optical depth measurements interpolated to the MODIS wavelengths using the fits shown in Figure 12. Bars show measurement uncertainties. .

Figure 14 Comparison of 380-nm wavelength aerosol optical depth measured by AATS-6 during aircraft horizontal flight legs at altitudes 30-100 m above the ocean surface, and corresponding 380-nm aerosol optical depth retrieved from TOMS ultraviolet backscatter measurements taken within 150 km and one hour of the AATS-6 data: (a) AOD values and uncertainties, (b) AOD differences (TOMS minus AATS-6) and combined measurement uncertainties.

Figure 15 Comparison of GOES-8 AOD retrievals in the GOES visible channel and AATS-6 measurements taken within 100 m of the ocean surface at the time of satellite observation and interpolated to 670 nm wavelength: (a) AOD values, measurement uncertainties, and spatio-temporal sample standard deviations, (b) AOD differences (GOES-8 minus AATS-6) and combined measurement uncertainties.

Figure 16 Observation of an AOD latitudinal gradient measured by AATS-6 (interpolated to 670 nm wavelength) and retrieved from GOES-8 measurements on 10 July. Dashed red lines represent a GOES-8 uncertainty of ±0.06; dotted red lines show sample standard deviations (see text for discussion). Dotted blue lines display the AATS-6 measurement uncertainties.

Figure 1

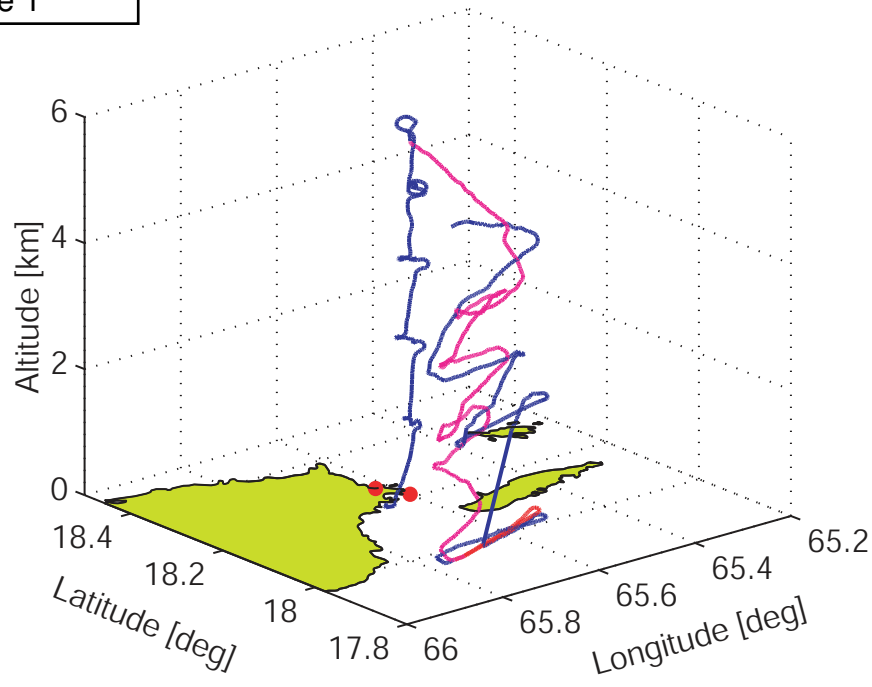
Altitude [km]
Latitude [deg]
Longitude [deg]

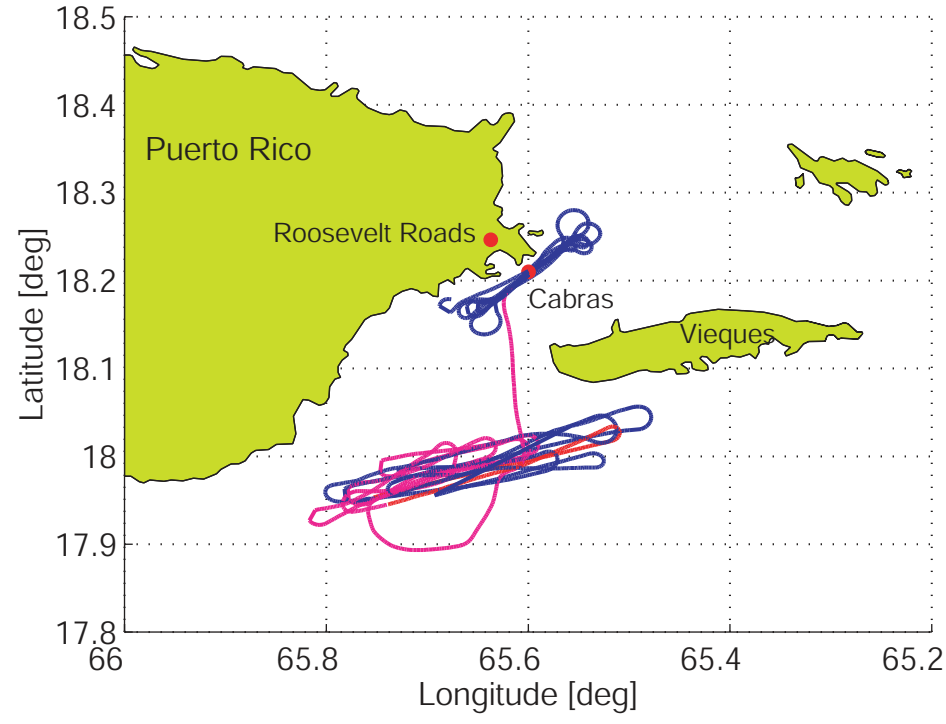
Puerto Rico
Roosevelt Roads
Cabras
Vieques
Latitude [deg]
Longitude [deg]

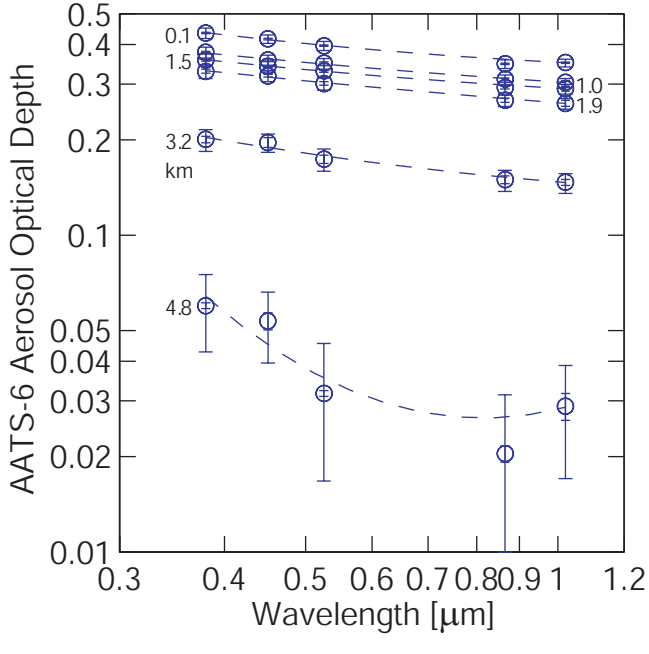
AATS-6 Aerosol Optical Depth
Wavelength [μm]
0.1
1.5
3.2
km
4.8
1.0
1.9

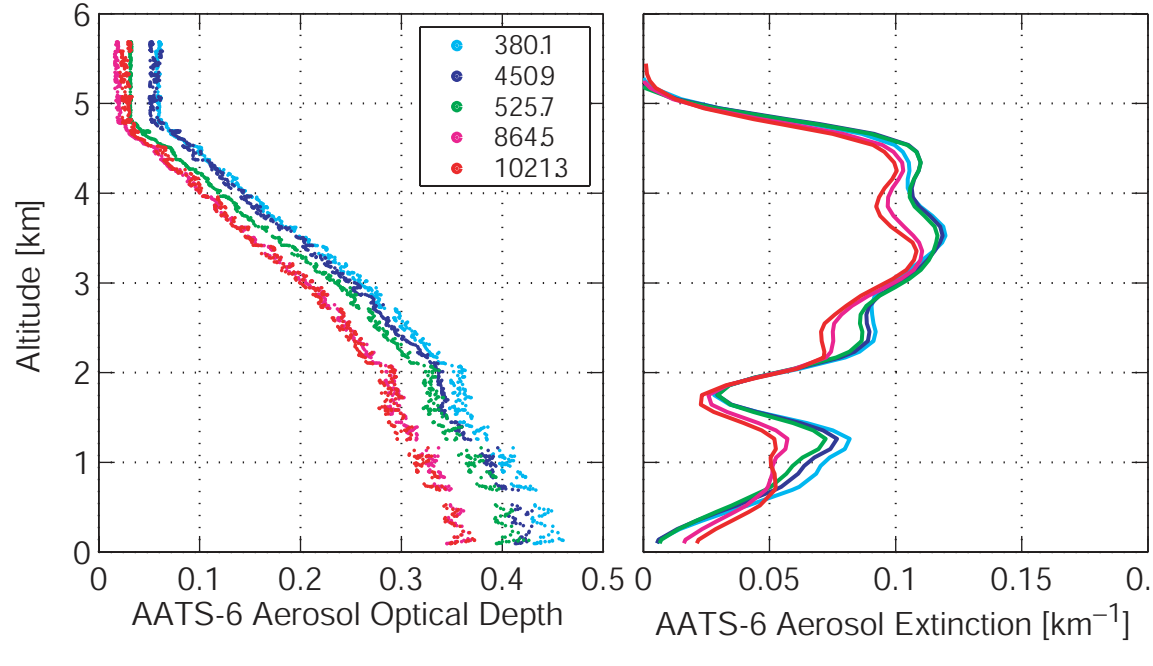
Altitude [km]
AATS-6 Aerosol Optical Depth
AATS-6 Aerosol Extinction [km^{-1}]
380.1
450.9
525.7
864.5
1021.3

Figure 2

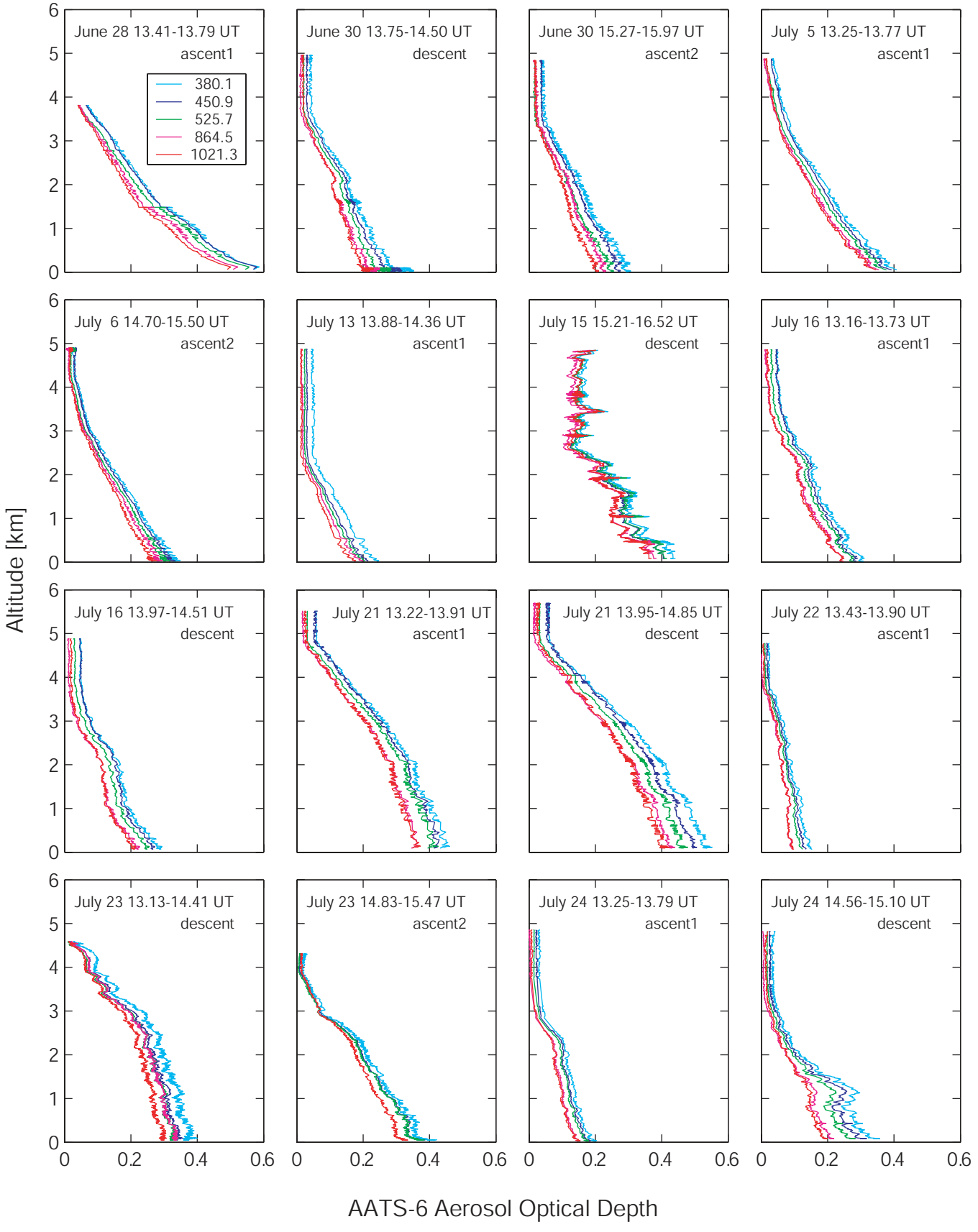
June 28 13.41-13.79 UT
ascent1
380.1
450.9
525.7
864.5
1021.3
June 30 13.75-14.50 UT
descent
June 30 15.27-15.97 UT
ascent2
July 5 13.25-13.77 UT
ascent1
July 6 14.70-15.50 UT
ascent2
July 13 13.88-14.36 UT
ascent1
July 15 15.21-16.52 UT
descent
July 16 13.16-13.73 UT
ascent1
July 16 13.97-14.51 UT
descent
July 21 13.22-13.91 UT
ascent1
July 21 13.95-14.85 UT
descent
July 22 13.43-13.90 UT
ascent1
July 23 13.13-14.41 UT
descent
July 23 14.83-15.47 UT
ascent2
July 24 13.25-13.79 UT
ascent1
July 24 14.56-15.10 UT
descent
Altitude [km]
AATS-6 Aerosol Optical Depth
0
1
2
3
4
5
6
0.2
0.4
0.6

Figure 3

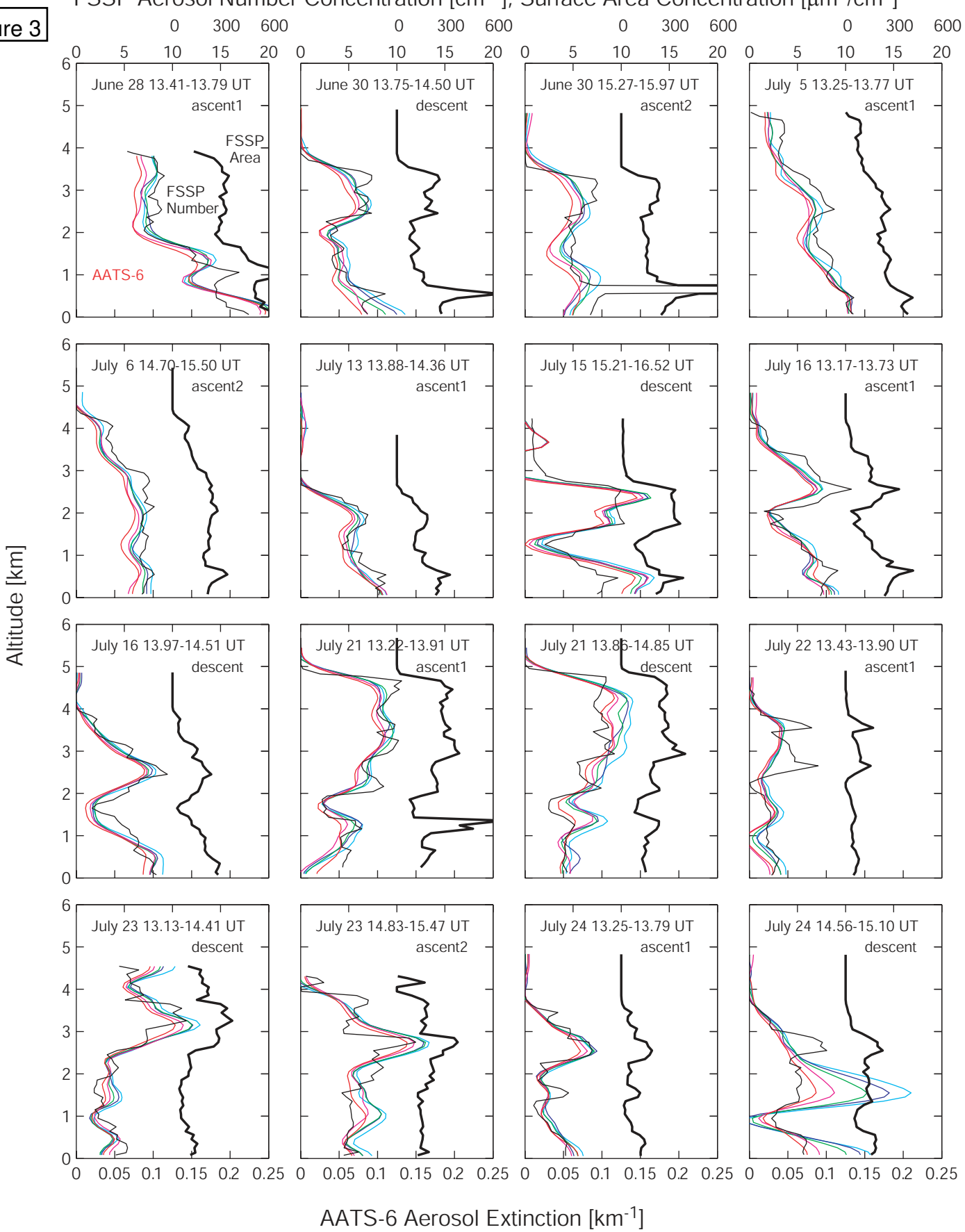
FSSP Aerosol Number Concentration [cm-3], Surface Area Concentration [μm2/cm3]
0 300 600
0 5 10 15 20
June 28 13.41-13.79 UT
ascent1
FSSP Area
FSSP Number
AATS-6
June 30 13.75-14.50 UT
descent
June 30 15.27-15.97 UT
ascent2
July 5 13.25-13.77 UT
ascent1
July 6 14.70-15.50 UT
ascent2
July 13 13.88-14.36 UT
ascent1
July 15 15.21-16.52 UT
descent
July 16 13.17-13.73 UT
ascent1
July 16 13.97-14.51 UT
descent
July 21 13.22-13.91 UT
ascent1
July 21 13.86-14.85 UT
descent
July 22 13.43-13.90 UT
ascent1
July 23 13.13-14.41 UT
descent
July 23 14.83-15.47 UT
ascent2
July 24 13.25-13.79 UT
ascent1
July 24 14.56-15.10 UT
descent
Altitude [km]
0 1 2 3 4 5 6
0 0.05 0.1 0.15 0.2 0.25
AATS-6 Aerosol Extinction [km-1]

Figure 4

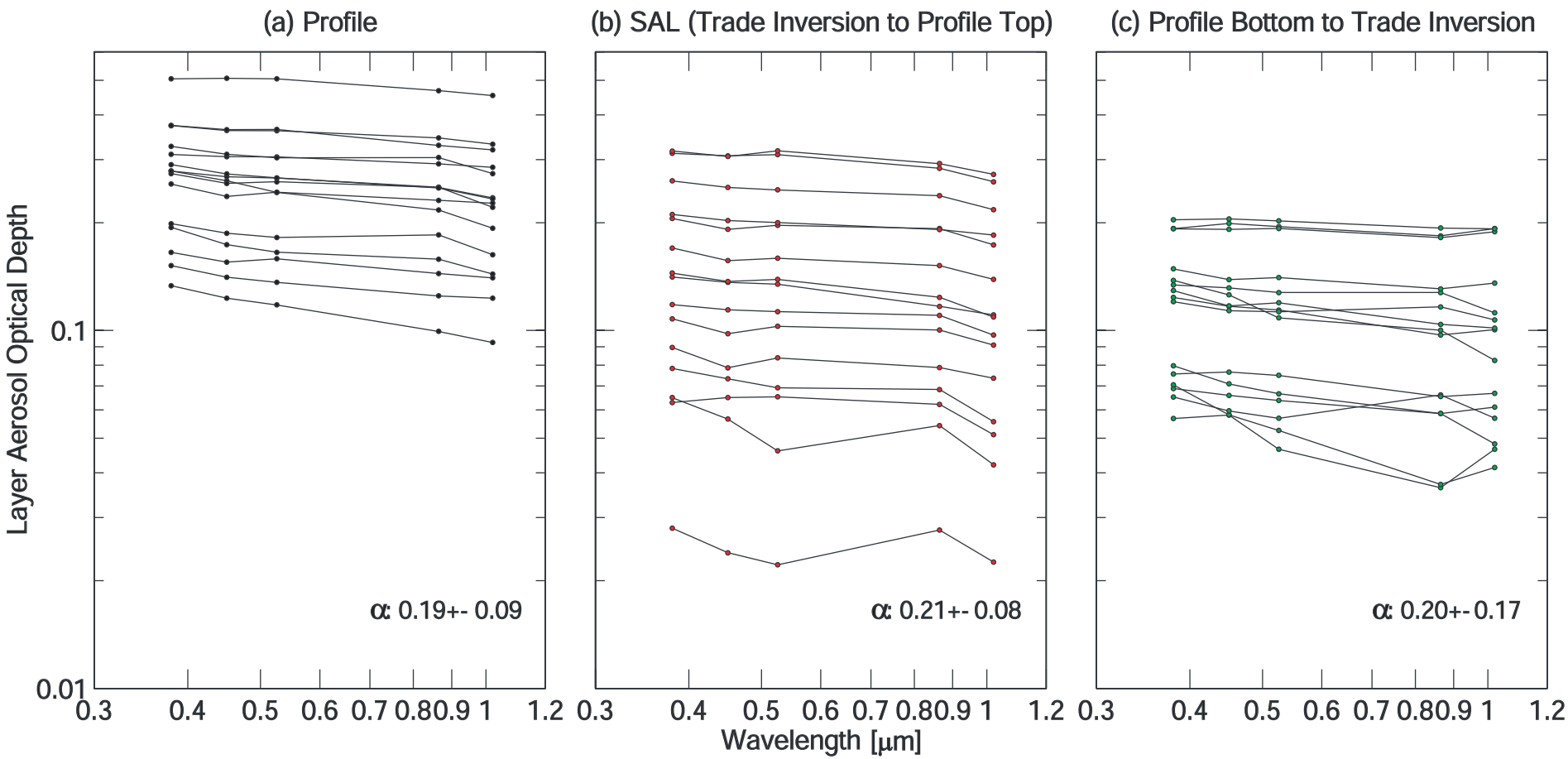
(a) Profile
(b) SAL (Trade Inversion to Profile Top)
(c) Profile Bottom to Trade Inversion
Layer Aerosol Optical Depth
0.1
0.01
α: 0.19+- 0.09
α: 0.21+- 0.08
α: 0.20+- 0.17
0.3 0.4 0.5 0.6 0.7 0.8 0.9 1 1.2
Wavelength [μm]

Figure 5

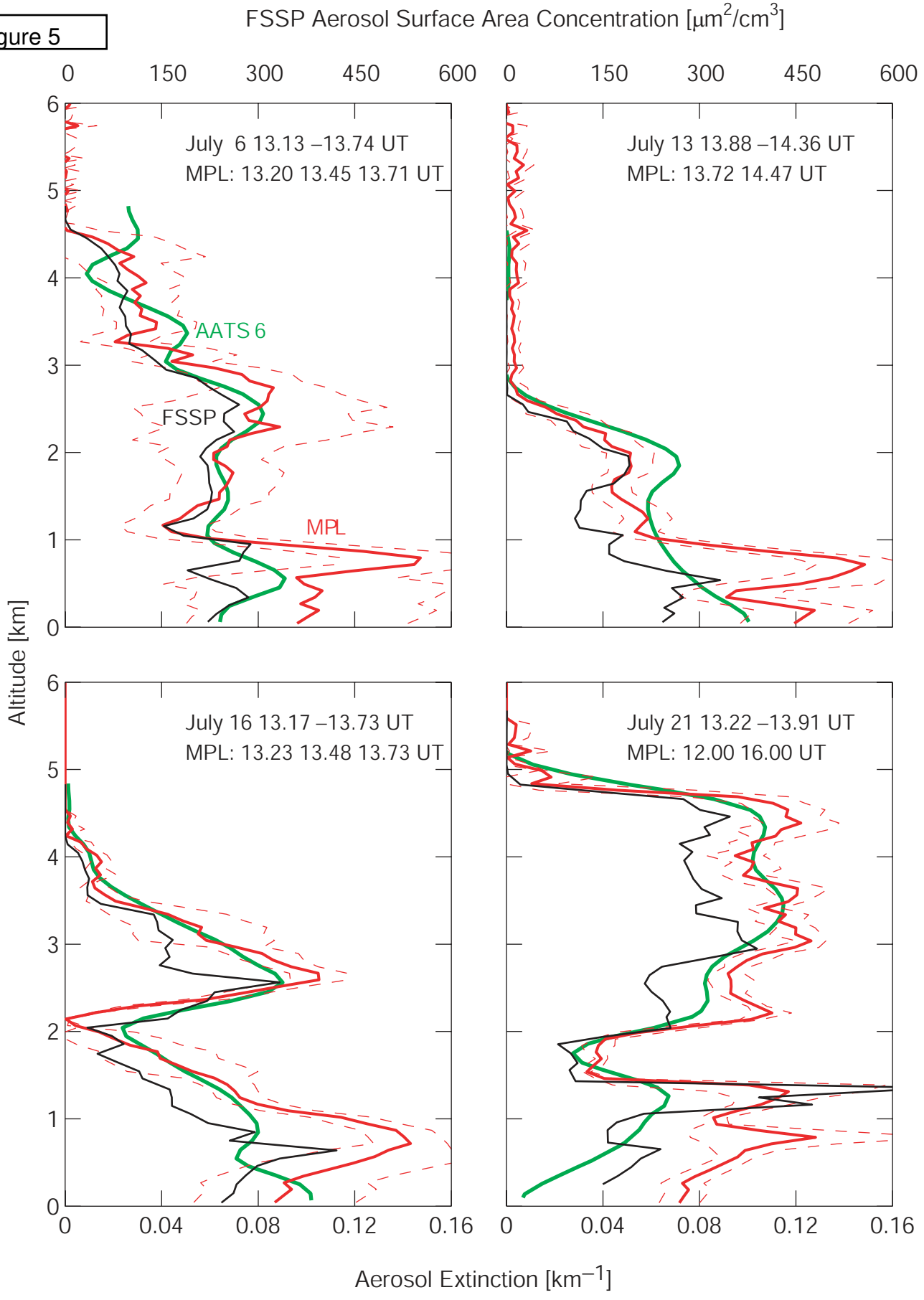
FSSP Aerosol Surface Area Concentration [μm²/cm³]
0
150
300
450
600
July 6 13.13 –13.74 UT
MPL: 13.20 13.45 13.71 UT
AATS 6
FSSP
MPL
July 13 13.88 –14.36 UT
MPL: 13.72 14.47 UT
July 16 13.17 –13.73 UT
MPL: 13.23 13.48 13.73 UT
July 21 13.22 –13.91 UT
MPL: 12.00 16.00 UT
Altitude [km]
0
1
2
3
4
5
6
0.04
0.08
0.12
0.16
Aerosol Extinction [km⁻¹]

Figure 6

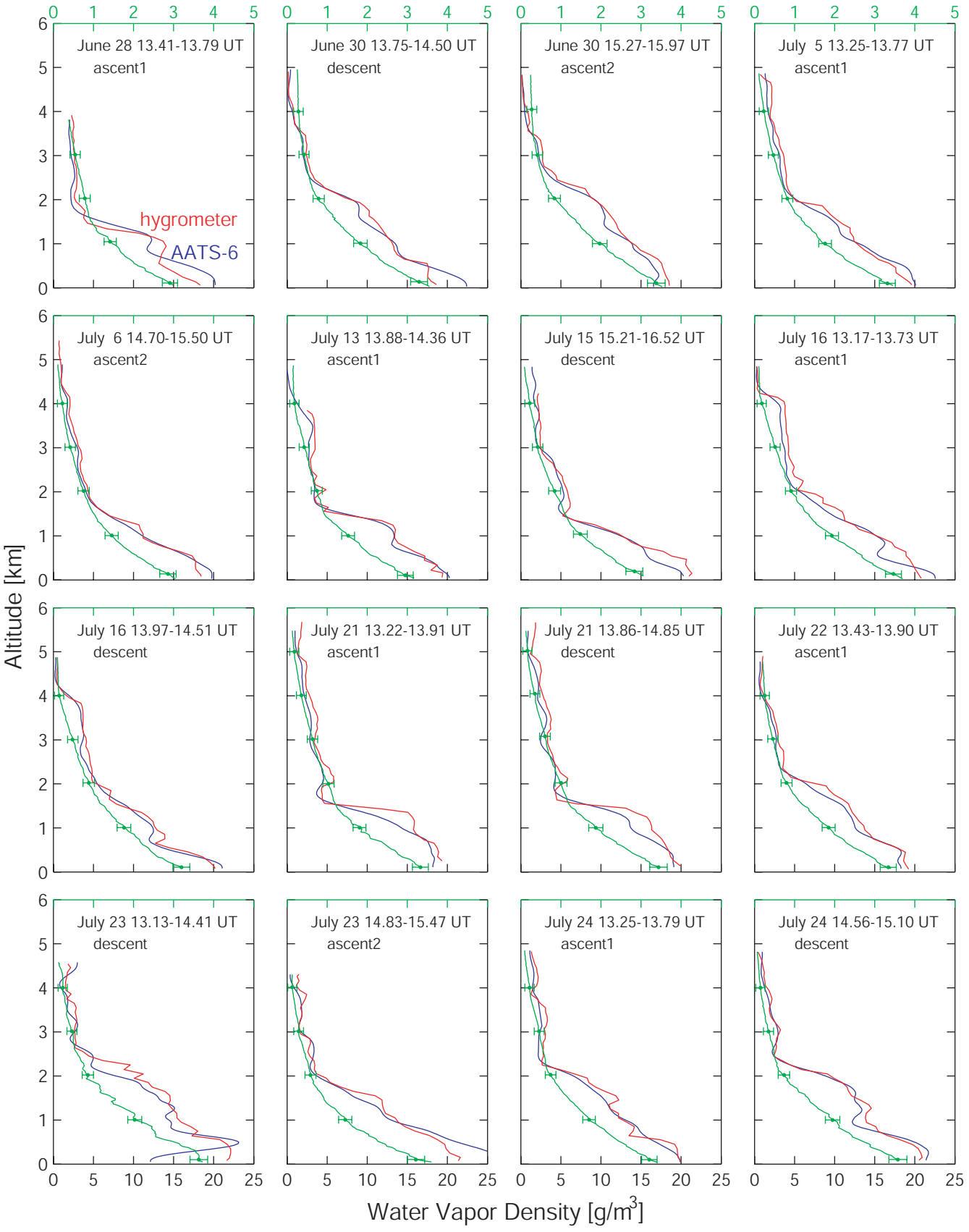
AATS-6 Columnar Water Vapor [g/cm^2]
June 28 13.41-13.79 UT
ascent1
hygrometer
AATS-6
June 30 13.75-14.50 UT
descent
June 30 15.27-15.97 UT
ascent2
July 5 13.25-13.77 UT
ascent1
July 6 14.70-15.50 UT
ascent2
July 13 13.88-14.36 UT
ascent1
July 15 15.21-16.52 UT
descent
July 16 13.17-13.73 UT
ascent1
July 16 13.97-14.51 UT
descent
July 21 13.22-13.91 UT
ascent1
July 21 13.86-14.85 UT
descent
July 22 13.43-13.90 UT
ascent1
July 23 13.13-14.41 UT
descent
July 23 14.83-15.47 UT
ascent2
July 24 13.25-13.79 UT
ascent1
July 24 14.56-15.10 UT
descent
Altitude [km]
Water Vapor Density [g/m^3]

Figure 7

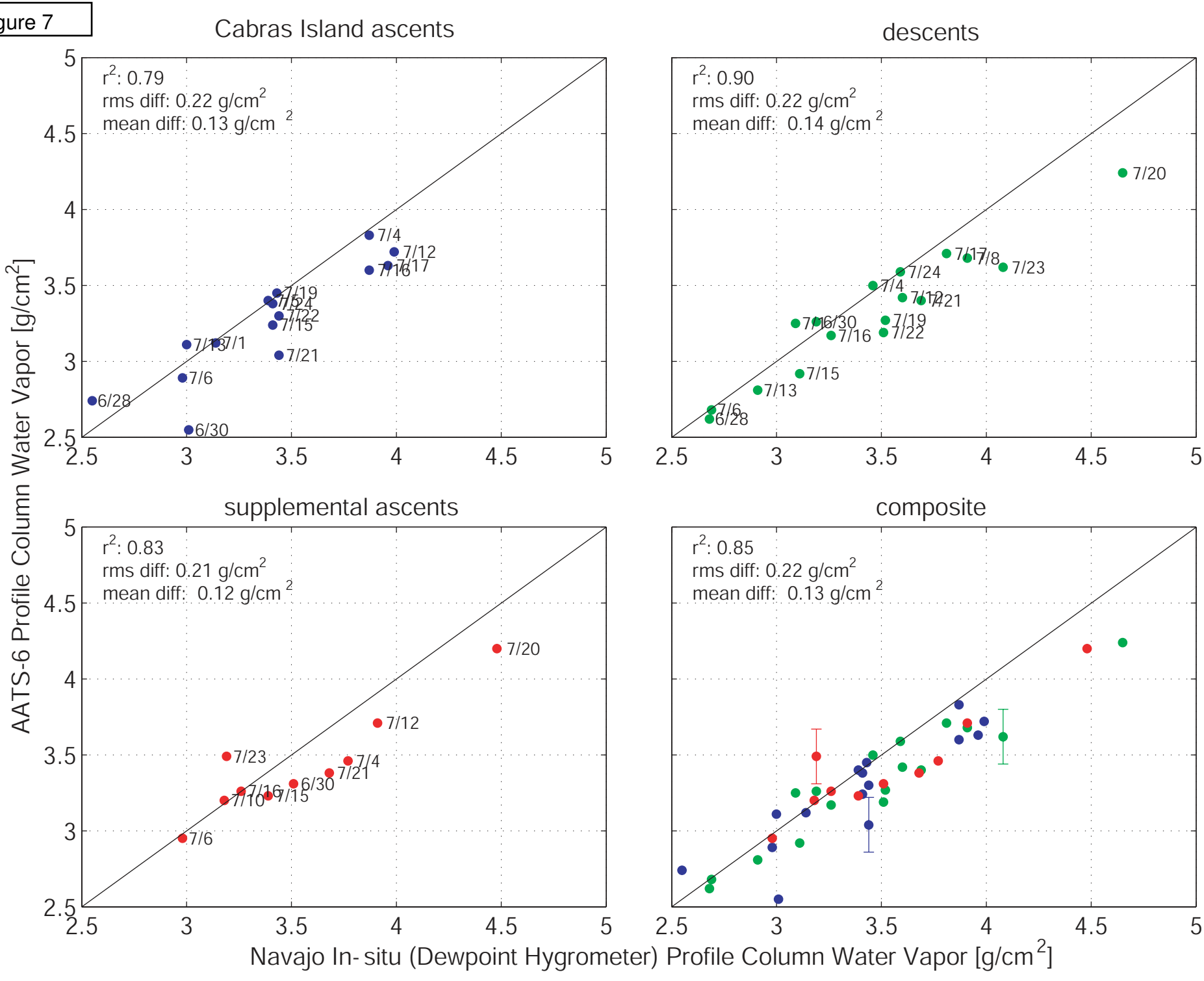
Cabras Island ascents
r2: 0.79
rms diff: 0.22 g/cm2
mean diff: 0.13 g/cm 2
7/4
7/12
7/16
7/17
7/19
7/24
7/22
7/15
7/13
7/1
7/21
7/6
6/28
6/30
descents
r2: 0.90
rms diff: 0.22 g/cm2
mean diff: 0.14 g/cm 2
7/20
7/17
7/8
7/23
7/24
7/4
7/12
7/21
7/16/30
7/19
7/16
7/22
7/15
7/13
7/6
6/28
supplemental ascents
r2: 0.83
rms diff: 0.21 g/cm2
mean diff: 0.12 g/cm 2
7/20
7/12
7/23
7/4
7/21
6/30
7/16
7/10
7/15
7/6
composite
r2: 0.85
rms diff: 0.22 g/cm2
mean diff: 0.13 g/cm 2
AATS-6 Profile Column Water Vapor [g/cm2]
Navajo In-situ (Dewpoint Hygrometer) Profile Column Water Vapor [g/cm2]

Figure 8

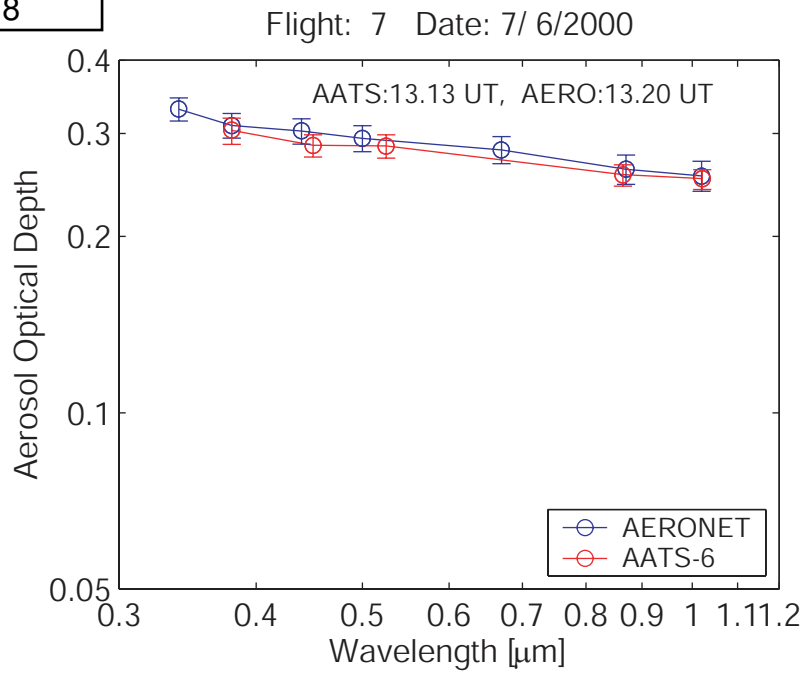
Flight: 7 Date: 7/ 6/2000
AATS:13.13 UT, AERO:13.20 UT
AERONET
AATS-6
Aerosol Optical Depth
Wavelength [μm]
0.4
0.3
0.2
0.1
0.05
0.3 0.4 0.5 0.6 0.7 0.8 0.9 1 1.1 1.2

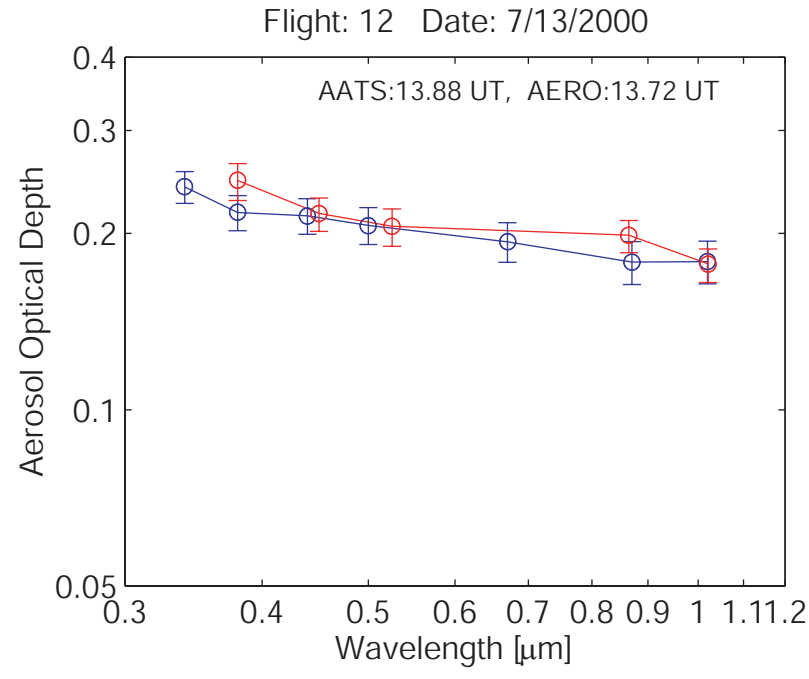
Flight: 12 Date: 7/13/2000
AATS:13.88 UT, AERO:13.72 UT
Aerosol Optical Depth
Wavelength [μm]
0.4
0.3
0.2
0.1
0.05
0.3 0.4 0.5 0.6 0.7 0.8 0.9 1 1.1 1.2

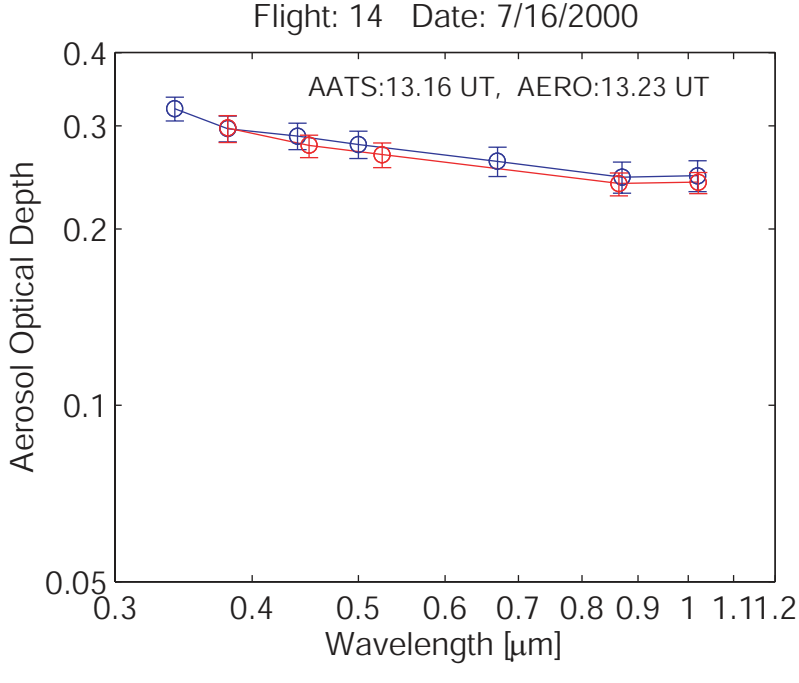
Flight: 14 Date: 7/16/2000
AATS:13.16 UT, AERO:13.23 UT
Aerosol Optical Depth
Wavelength [μm]
0.4
0.3
0.2
0.1
0.05
0.3 0.4 0.5 0.6 0.7 0.8 0.9 1 1.1 1.2

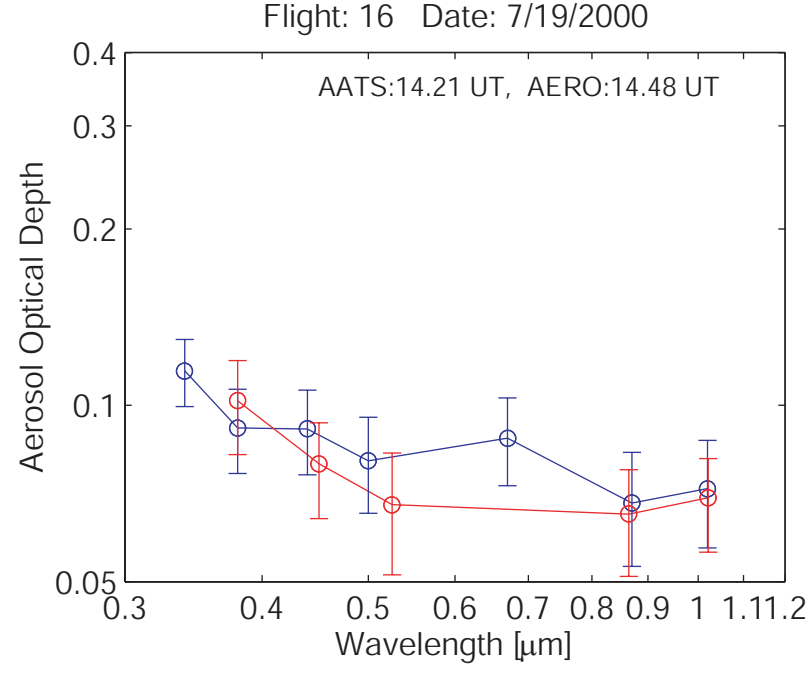
Flight: 16 Date: 7/19/2000
AATS:14.21 UT, AERO:14.48 UT
Aerosol Optical Depth
Wavelength [μm]
0.4
0.3
0.2
0.1
0.05
0.3 0.4 0.5 0.6 0.7 0.8 0.9 1 1.1 1.2

Figure 9

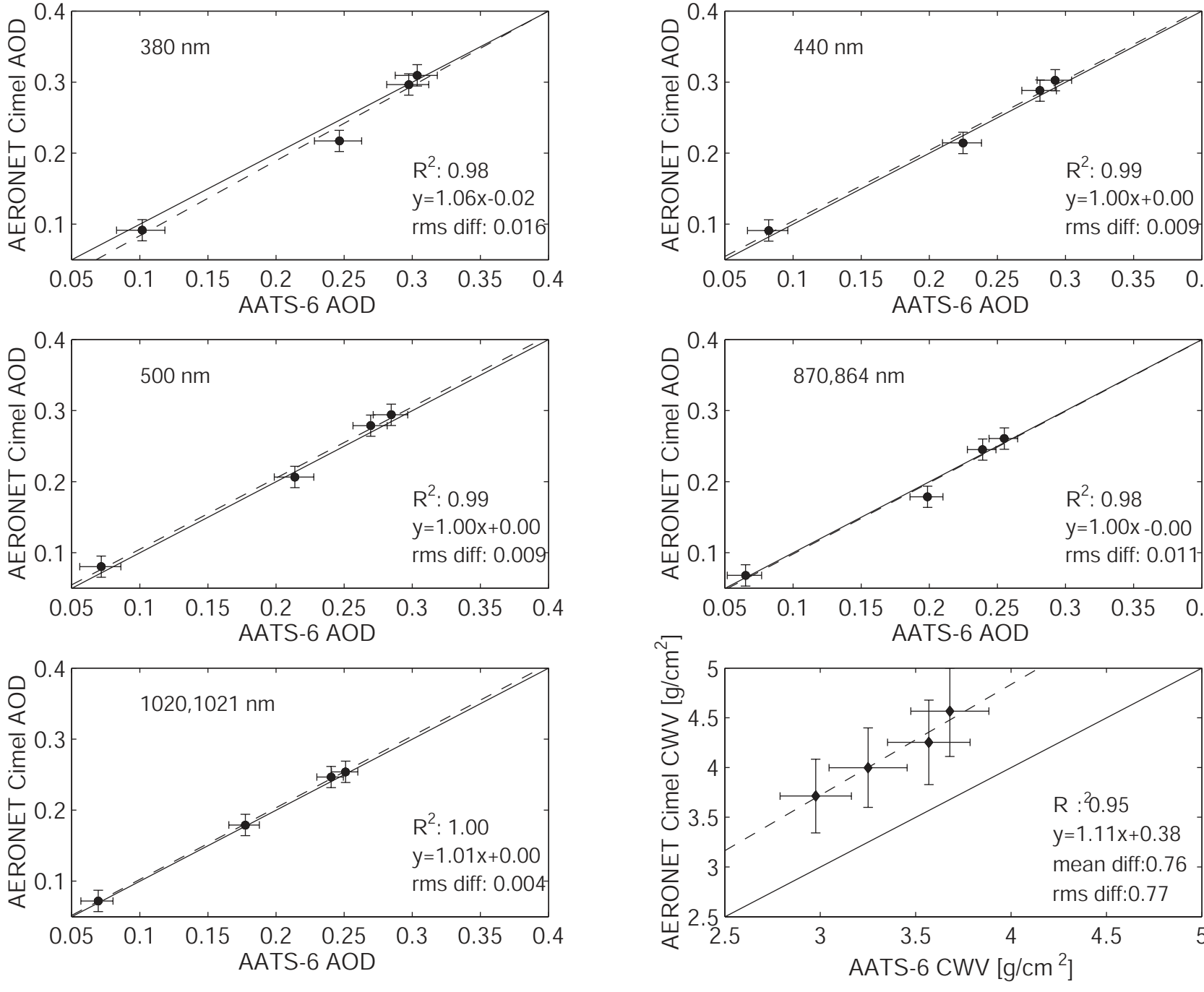
380 nm
R2: 0.98
y=1.06x-0.02
rms diff: 0.016
440 nm
R2: 0.99
y=1.00x+0.00
rms diff: 0.009
500 nm
R2: 0.99
y=1.00x+0.00
rms diff: 0.009
870,864 nm
R2: 0.98
y=1.00x -0.00
rms diff: 0.011
1020,1021 nm
R2: 1.00
y=1.01x+0.00
rms diff: 0.004
R :20.95
y=1.11x+0.38
mean diff:0.76
rms diff:0.77
AERONET Cimel AOD
AATS-6 AOD
AERONET Cimel CWV [g/cm2]
AATS-6 CWV [g/cm 2]

Figure 10

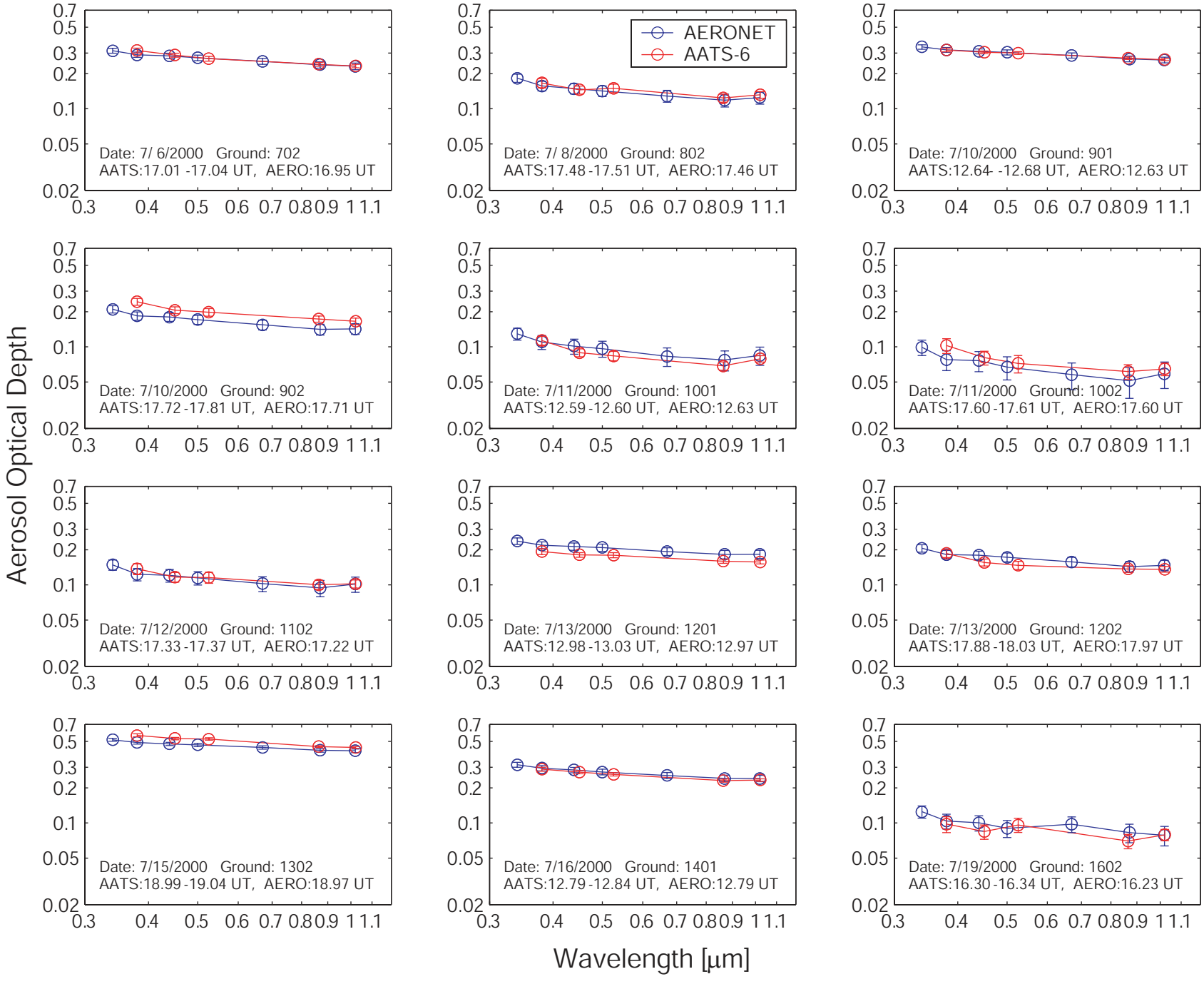
AERONET
AATS-6
Date: 7/ 6/2000 Ground: 702
AATS:17.01 -17.04 UT, AERO:16.95 UT
Date: 7/ 8/2000 Ground: 802
AATS:17.48 -17.51 UT, AERO:17.46 UT
Date: 7/10/2000 Ground: 901
AATS:12.64- -12.68 UT, AERO:12.63 UT
Date: 7/10/2000 Ground: 902
AATS:17.72 -17.81 UT, AERO:17.71 UT
Date: 7/11/2000 Ground: 1001
AATS:12.59 -12.60 UT, AERO:12.63 UT
Date: 7/11/2000 Ground: 1002
AATS:17.60 -17.61 UT, AERO:17.60 UT
Date: 7/12/2000 Ground: 1102
AATS:17.33 -17.37 UT, AERO:17.22 UT
Date: 7/13/2000 Ground: 1201
AATS:12.98 -13.03 UT, AERO:12.97 UT
Date: 7/13/2000 Ground: 1202
AATS:17.88 -18.03 UT, AERO:17.97 UT
Date: 7/15/2000 Ground: 1302
AATS:18.99 -19.04 UT, AERO:18.97 UT
Date: 7/16/2000 Ground: 1401
AATS:12.79 -12.84 UT, AERO:12.79 UT
Date: 7/19/2000 Ground: 1602
AATS:16.30 -16.34 UT, AERO:16.23 UT
Aerosol Optical Depth
Wavelength [μm]

Figure 11

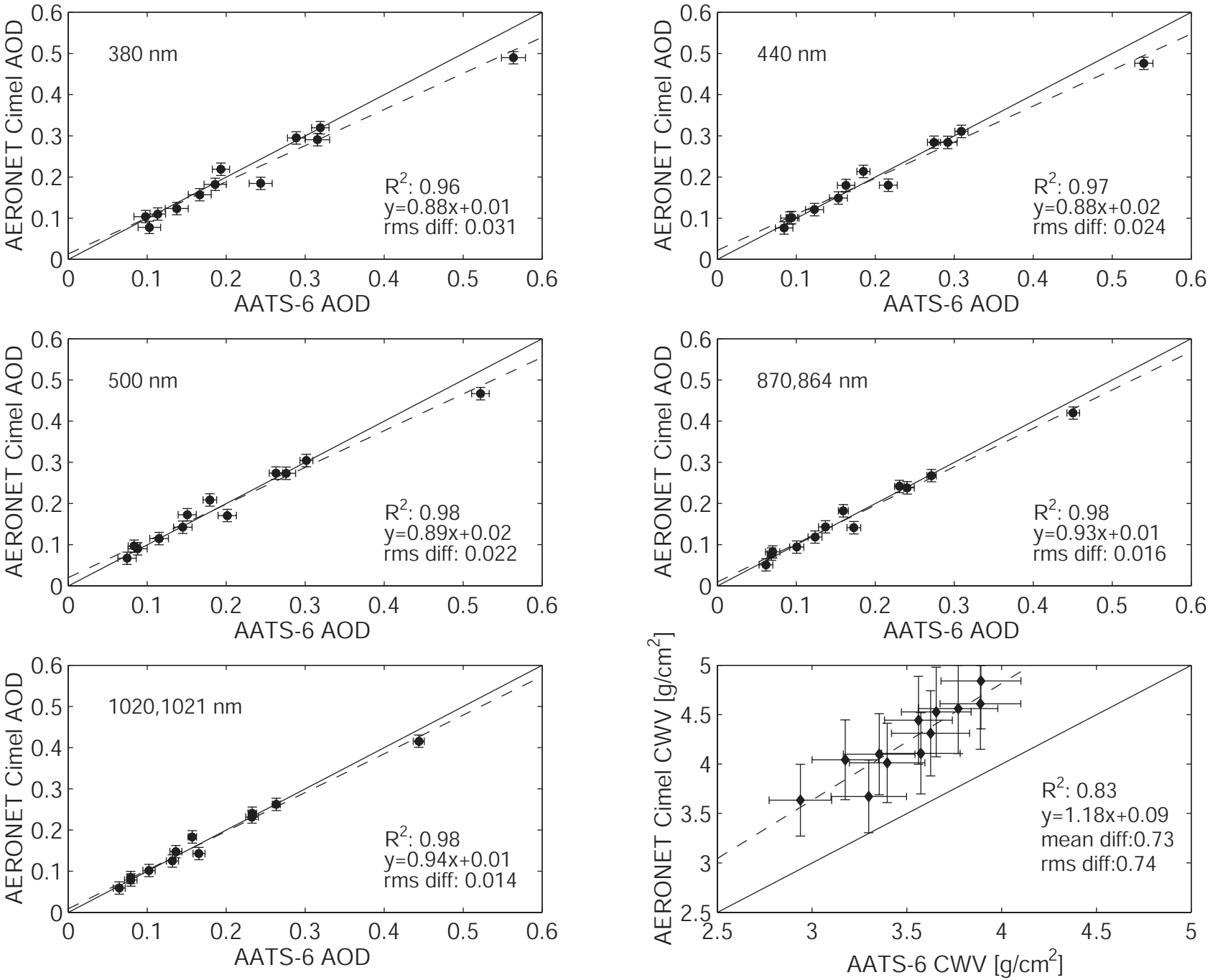
380 nm
R2: 0.96
y=0.88x+0.01
rms diff: 0.031
440 nm
R2: 0.97
y=0.88x+0.02
rms diff: 0.024
500 nm
R2: 0.98
y=0.89x+0.02
rms diff: 0.022
870,864 nm
R2: 0.98
y=0.93x+0.01
rms diff: 0.016
1020,1021 nm
R2: 0.98
y=0.94x+0.01
rms diff: 0.014
R2: 0.83
y=1.18x+0.09
mean diff:0.73
rms diff:0.74
AERONET Cimel AOD
AATS-6 AOD
AERONET Cimel CWV [g/cm2]
AATS-6 CWV [g/cm2]

Figure 12

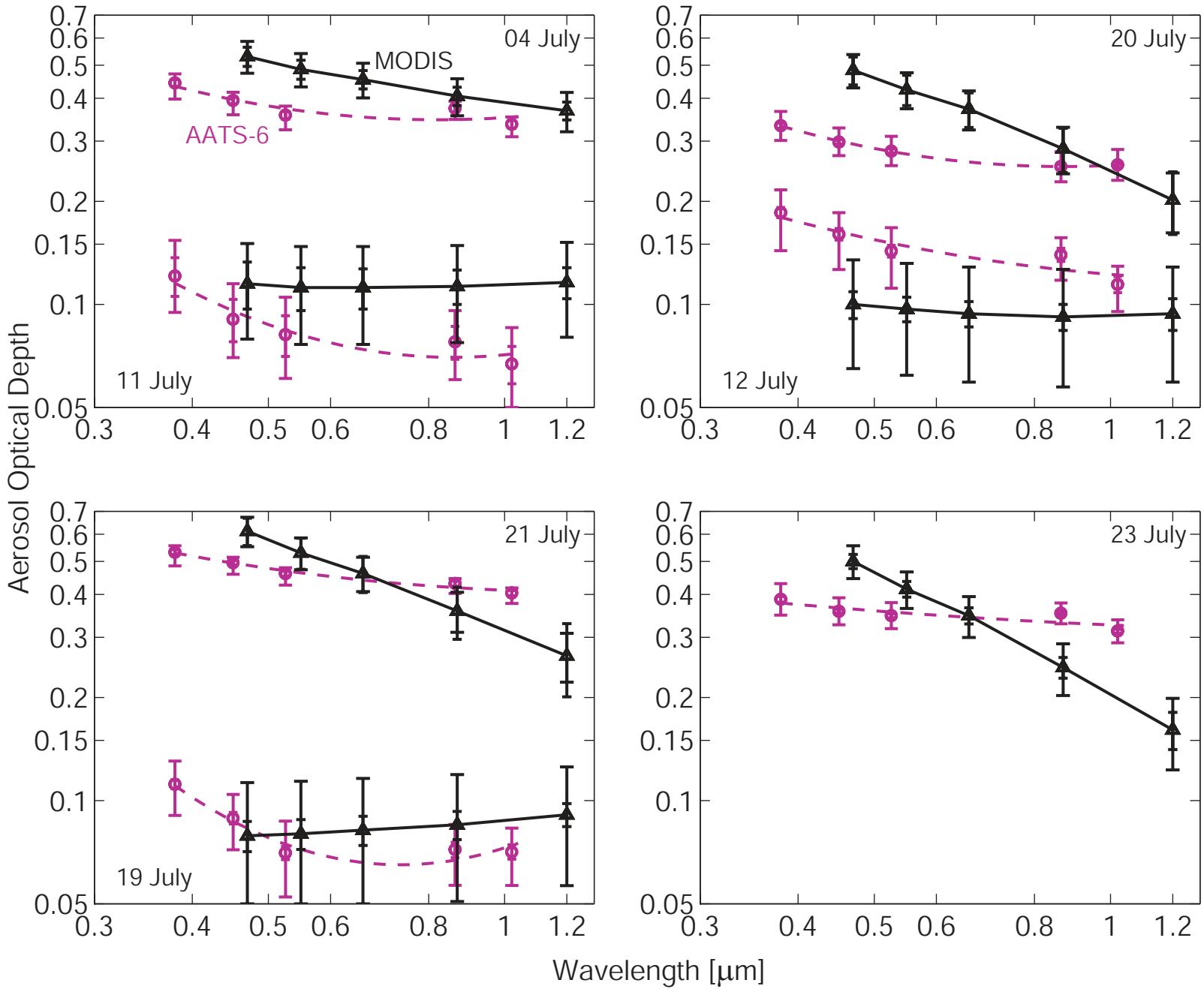
04 July
MODIS
AATS-6
11 July
20 July
12 July
21 July
19 July
23 July
Aerosol Optical Depth
Wavelength [μm]
0.7
0.6
0.5
0.4
0.3
0.2
0.15
0.1
0.05
0.3
0.4
0.5
0.6
0.8
1
1.2

Figure 13

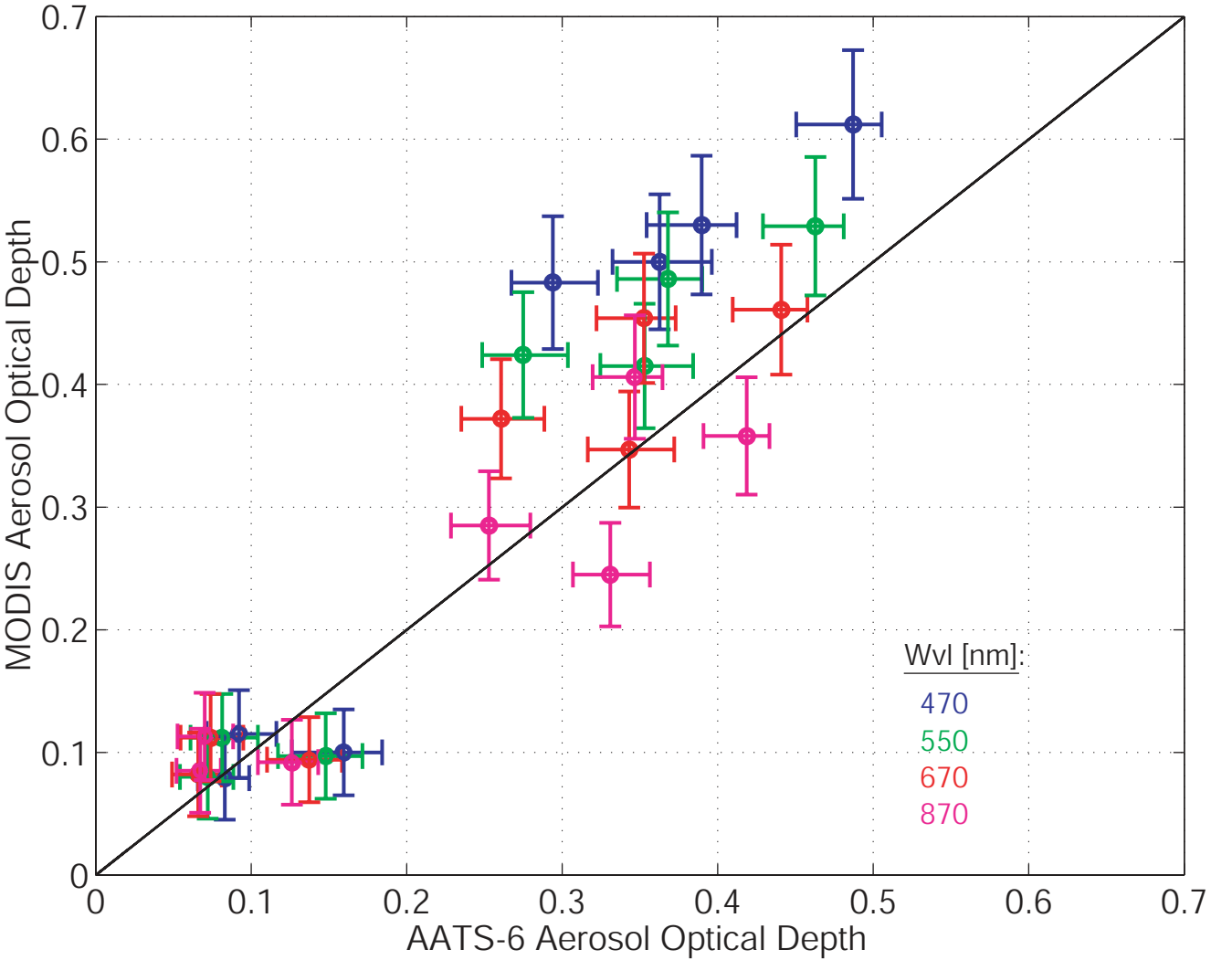
MODIS Aerosol Optical Depth
AATS-6 Aerosol Optical Depth
0
0.1
0.2
0.3
0.4
0.5
0.6
0.7
Wvl [nm]:
470
550
670
870

Figure 14

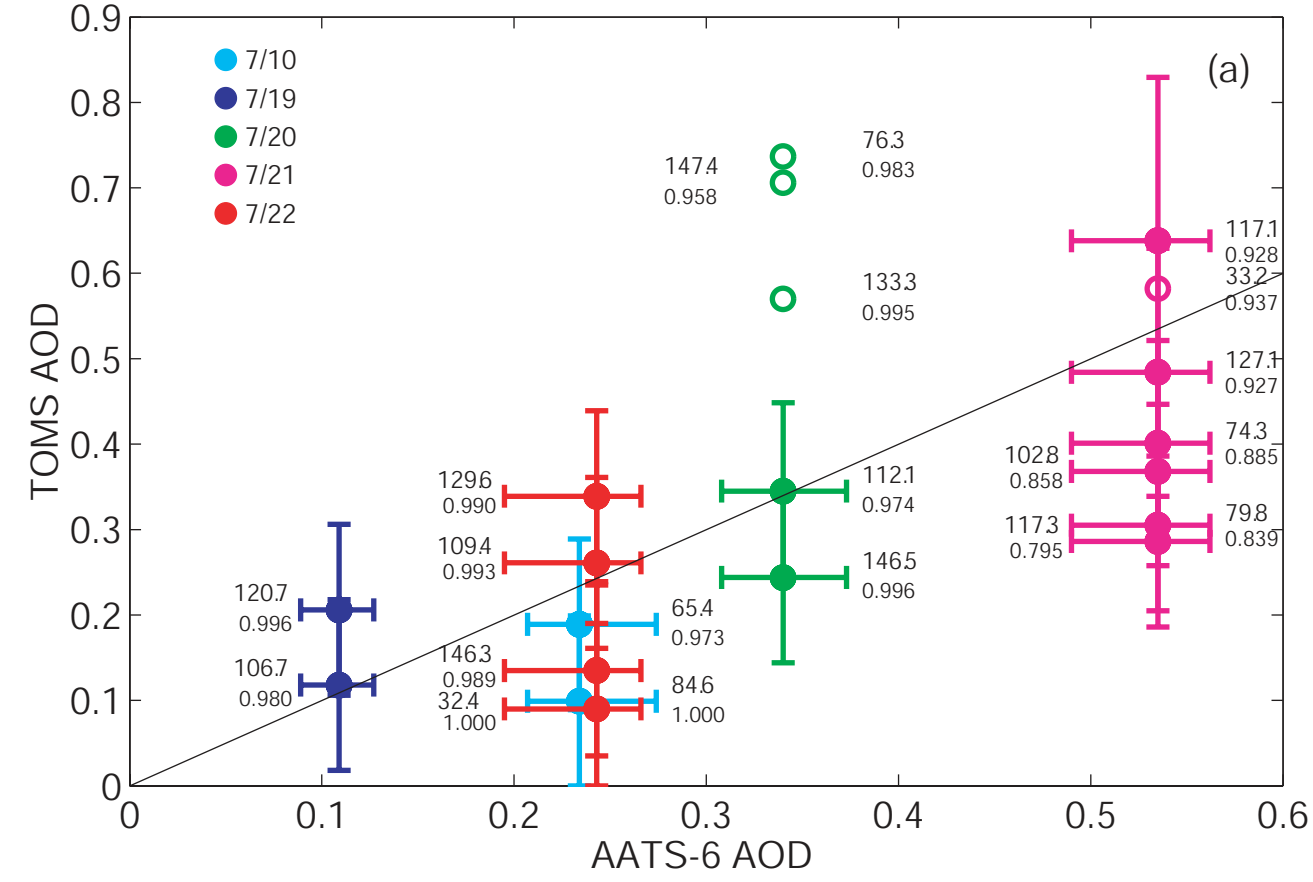
(a)
7/10
7/19
7/20
7/21
7/22
TOMS AOD
AATS-6 AOD
0
0.1
0.2
0.3
0.4
0.5
0.6
0.7
0.8
0.9
120.7
0.996
106.7
0.980
129.6
0.990
109.4
0.993
146.3
0.989
32.4
1.000
65.4
0.973
84.6
1.000
147.4
0.958
76.3
0.983
133.3
0.995
112.1
0.974
146.5
0.996
117.1
0.928
33.2
0.937
127.1
0.927
74.3
0.885
102.8
0.858
117.3
0.795
79.8
0.839

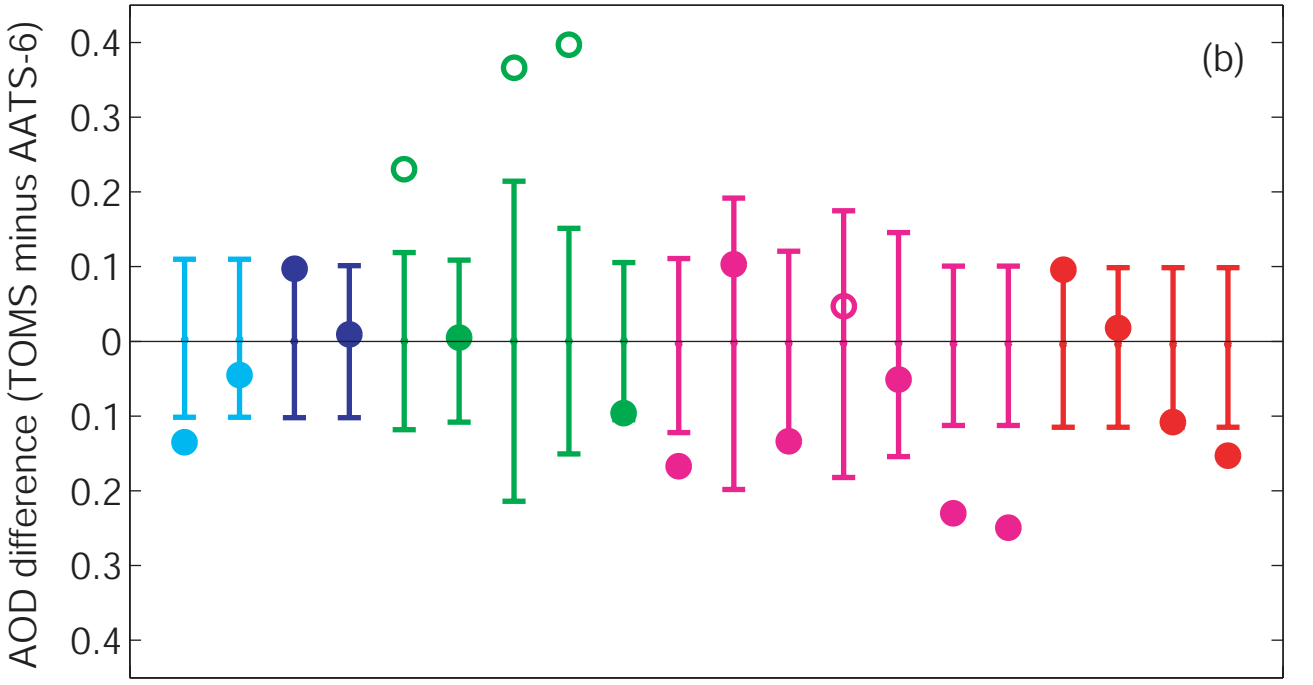
(b)
AOD difference (TOMS minus AATS-6)
0.4
0.3
0.2
0.1
0
0.1
0.2
0.3
0.4

Figure 15

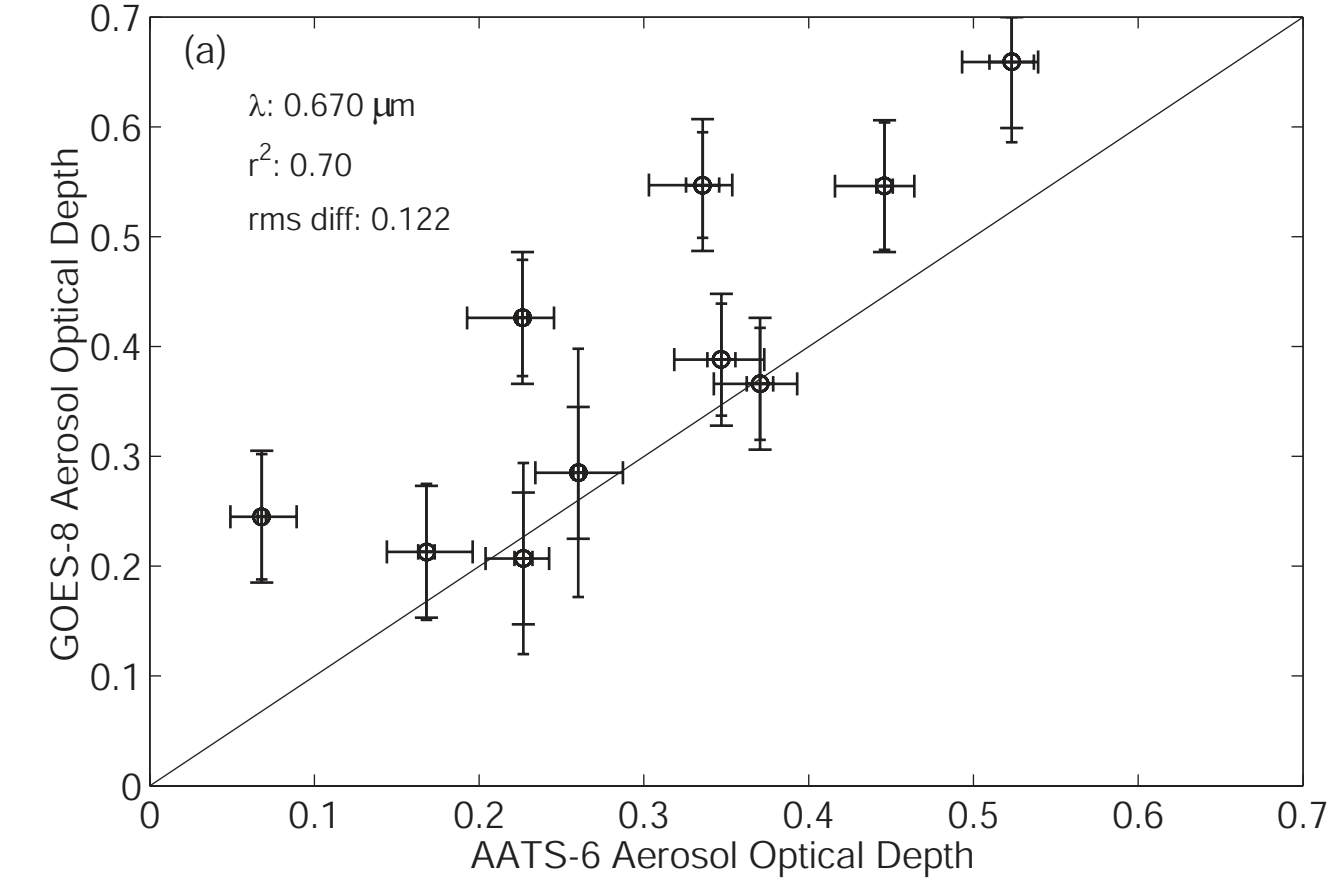
(a)
λ: 0.670 μm
r2: 0.70
rms diff: 0.122
GOES-8 Aerosol Optical Depth
AATS-6 Aerosol Optical Depth
0
0.1
0.2
0.3
0.4
0.5
0.6
0.7

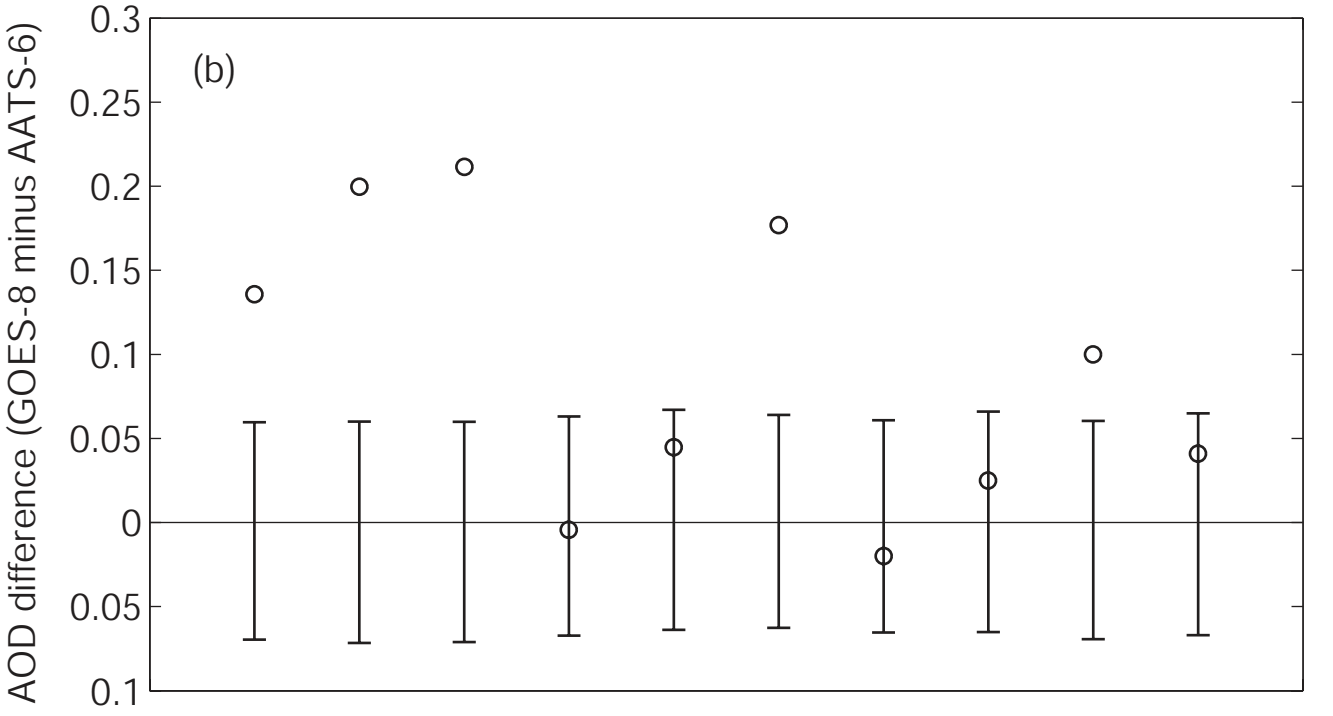
(b)
AOD difference (GOES-8 minus AATS-6)
0.3
0.25
0.2
0.15
0.1
0.05
0
0.05
0.1

Figure 16

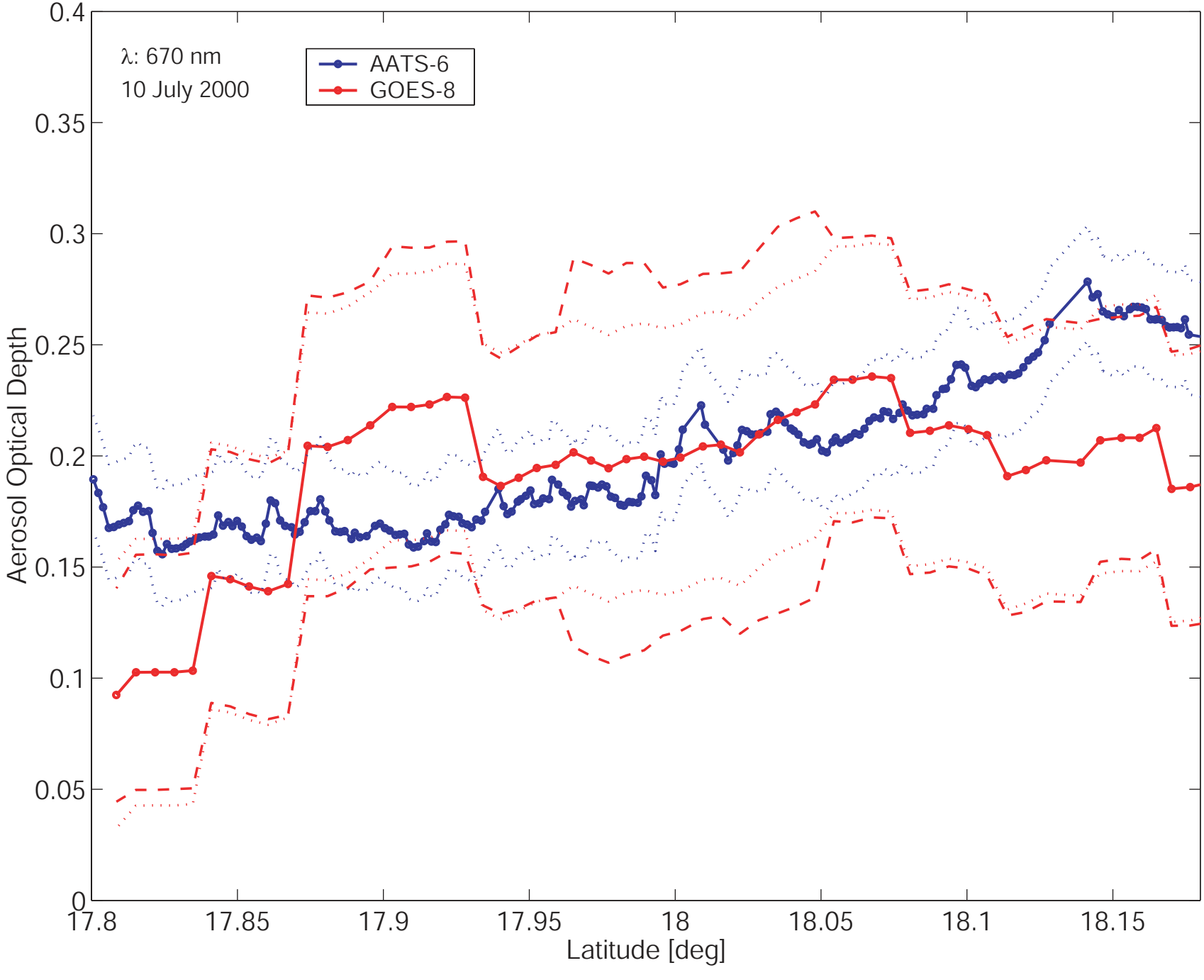
λ: 670 nm
10 July 2000
AATS-6
GOES-8
Aerosol Optical Depth
0.4
0.35
0.3
0.25
0.2
0.15
0.1
0.05
0
17.8
17.85
17.9
17.95
18
18.05
18.1
18.15
Latitude [deg]